

Universal polarization energies for defects in monolayer, surface and bulk hexagonal boron nitride : A finite-size fragments *GW* approach

David Amblard,¹ Gabriele D'Avino,¹ Ivan Duchemin,² and Xavier Blase¹

¹*Univ. Grenoble Alpes, CNRS, Inst NEEL, F-38042 Grenoble, France*

²*Univ. Grenoble Alpes, CEA, IRIG-MEM-L_Sim, 38054 Grenoble, France*

Abstract

We study defect energy levels in hexagonal boron-nitride with varying number of layers using a fragment many-body *GW* formalism, taking as examples the paradigmatic carbon-dimer and $C_B V_N$ defects. We show that a single layer can be fragmented in polarizable finite-size areas reproducing faithfully the effect of the dielectric environment, dramatically facilitating the study at the many-body level of point defects in the dilute limit. The evolution of defect energy levels from the monolayer to a n -layer system due to increased screening, labeled polarization energies, follow a simple $(\Delta P/n + P_\infty)$ behavior. The coefficients ΔP and P_∞ are found to be close-to-universal, with opposite signs for holes and electrons, characterizing mainly the host and the position of the defect (surface or bulk), but hardly the defect type. Our results rationalize the evolution of defect energy levels with layers number, allowing to safely extrapolate results obtained for the monolayer to few-layers, surface or bulk h -BN. The present many-body fragment approach further opens the door to studying disordered 2D layers.

I. INTRODUCTION

Defects in hexagonal boron-nitride (*h*-BN) have generated much research activity both at the experimental [1–13] and theoretical [14–38] level to better understand their unique photoluminescent properties. The large gap of the host *h*-BN allows a variety of localized occupied and unoccupied defect states controlling the absorption and emission spectrum across the visible range. While the optical properties of defects can be used as a way to unravel their chemical nature, thanks to the comparison between theoretical and experimental optical emission energies and lineshapes, much less is known experimentally about their electronic energy levels as measured by photoemission. Still, optical properties are strongly related to an accurate description of defect electronic properties, together with the strength of the excitonic electron-hole screened interaction. Further, the position of the defect energy levels in the host gap, in conjunction with structural reorganization energies, allows to predict its charge state as a function of the chemical potential.

The exploration of the electronic properties of defects in the dilute limit using *ab initio* simulations remains a difficult task. The most common periodic boundary condition (PBC) calculations, with defects repeated periodically, requires rather large unit cells to minimize spurious defect-defect interactions. This is all the more a difficulty in the case of charged defects for which Coulomb truncation techniques must be used to annihilate long-range Coulomb interactions between periodic images [39]. Further, at the efficient density-functional theory (DFT) Kohn-Sham level, the position of the electronic energy levels is known to be strongly sensitive to the choice of the exchange-correlation functional, limiting the predictive character of the related calculations. In the absence of experimental photoemission data characterizing defect levels, this may lead to difficulties on the best strategy to adopt. Recently, a scheme based on enforcing Koopman’s like conditions [40] illustrated the importance of changing the amount of exact exchange at the generalized Kohn-Sham DFT level as a function of the number of *h*-BN layers [25].

In the family of techniques going beyond Kohn-Sham DFT for the study of electronic energy levels, the many-body Green’s function *GW* perturbation theory [41–45] stands as a now common approach offering a reasonable compromise between accuracy and computer cost. Following pioneering studies for defects in 3D systems [46–51], *GW* calculations for defects in cubic [52] and hexagonal [14–17, 25, 31, 36–38] BN have been conducted in a few groups. Of specific interest for the present study, such a formalism accounts for the interaction of an added charge with the *N*-electron system, properly mimicking a photoemission experiment. This interaction is

constructed using the calculated linear-response electronic susceptibility that adapts to the dielectric environment. As such, the related screened Coulomb potential W fully accounts for the change in dielectric conditions from the monolayer to the few-layers or bulk limit.

As a caveat of properly accounting for charging effects, GW calculations with periodic boundary conditions also encounters difficulties associated with spurious long-range Coulomb interactions between images in the case of periodic boundary calculations. As recently analyzed in the case of defected h -BN systems [17], 2D GW calculations converge slowly, both with the amount of vacuum between repeated images and with the in-plane unit-cell size. While Coulomb truncation techniques can be used to avoid spurious interlayer interactions for the monolayer limit [17, 53, 54], eliminating interactions between periodically repeated defects within a layer, without affecting the in-plane screening by the h -BN host, stands as a difficult challenge. In the bulk limit, the necessity to include a sufficient number of pristine layers in the c -axis direction further increases computational cost. As a matter of fact, GW calculations for defects in h -BN were conducted essentially for monolayers [14, 16, 17, 25, 31, 36, 38], with one study of defected 3-layer systems [25] and one bulk study with 2-layers per unit-cell [37].

We propose in the present work an alternative finite-size cluster approach, performing GW calculations of defect energy levels in h -BN, reaching the monolayer, few-layers, surface and bulk dilute limit conditions. Defected and pristine flakes with increasing lateral size are stacked, reaching sizes large enough to safely extrapolate to the infinite limit for a given number of layers. We show that convergence with respect to in-plane dimensions can be dramatically facilitated by adopting a fragment scheme where each layer is reconstructed by patching large h -BN clusters, neglecting wavefunctions overlap between fragments on the same or neighboring layers. This allows to study at the many-body level systems containing several thousand atoms, reaching sizes large enough to reliably extrapolate to the infinite 2D or 3D limits. Defect energy level variations from the monolayer to a n -layer system follow a simple $(\Delta P/n + P_\infty)$ polarization energy behavior, where the rate and asymptotic coefficients ΔP and P_∞ characterize mainly the host and the position of the defect (surface or bulk), but hardly the defect type. Our study rationalizes the evolution of defect energy levels as a function of the number of layers. As a result, data obtained for the monolayer, or very-few layer systems, can be easily extrapolated to the surface or bulk limit without the need to perform additional many-body calculations.

II. METHODOLOGY

We briefly outline in this Section the methodology adopted in the present study. More details on the GW formalism [41–45] can be found in the thorough reviews written on the subject [55–60]. Let’s recall for the present purpose that the poles of the one-body Green’s function G represent by definition proper electron addition $E_n[N + 1] - E_0[N]$ or removal $E_0[N] - E_n[N - 1]$ energies, with $E_n[N \pm 1]$ the total energy of the $(N \pm 1)$ electron system in its n -th excited state, and $E_0[N]$ the ground-state energy of the N -electron system. As such, the poles of the Green’s function account for the interaction of an added charge with the rest of the system, including with a polarizable environment through its contribution to the screened Coulomb potential W . While the price of calculating the screened Coulomb potential for large multilayer systems in the dilute defect limit is prohibitively expensive, the fragment approach that neglects wavefunction overlaps between layers, and further between subsections of a same layer, leads to a dramatic cost reduction with small induced errors.

A. Fragment GW calculations

We restrict ourselves to define the quantities of interest in the present paper, namely the GW self-energy and the screened Coulomb potential W . The GW self-energy represents an approximation to the dynamical exchange-correlation operator that appears in the equation-of-motion for the time-ordered one-body Green’s function G , with:

$$\Sigma^{GW}(\mathbf{r}, \mathbf{r}'; E) = \frac{i}{2\pi} \int d\omega e^{i\omega\eta} G(\mathbf{r}, \mathbf{r}'; E + \omega) W(\mathbf{r}, \mathbf{r}'; \omega) \quad (1)$$

$$W(\mathbf{r}, \mathbf{r}'; \omega) = v(\mathbf{r}, \mathbf{r}') + \int d\mathbf{r}_1 d\mathbf{r}_2 v(\mathbf{r}, \mathbf{r}_1) \chi_0(\mathbf{r}_1, \mathbf{r}_2; \omega) W(\mathbf{r}_2, \mathbf{r}'; \omega) \quad (2)$$

$$\chi_0(\mathbf{r}, \mathbf{r}'; \omega) = \sum_{mn} (f_m - f_n) \frac{\phi_n^*(\mathbf{r}) \phi_m(\mathbf{r}) \phi_m^*(\mathbf{r}') \phi_n(\mathbf{r}')}{\omega - (\varepsilon_m - \varepsilon_n) + i\eta} \quad (3)$$

where χ_0 is the independent-electron susceptibility and v the bare Coulomb potential. The terms $\{f_{n/m}\}$ are level occupation factors and η a positive infinitesimal. In practice, the needed input Green’s function G and susceptibility χ_0 are calculated with input $\{\varepsilon_n^{KS}, \phi_n^{KS}\}$ Kohn-Sham eigenstates, e.g.:

$$G^{KS}(\mathbf{r}, \mathbf{r}'; \omega) = \sum_n \frac{\phi_n^{KS}(\mathbf{r}) [\phi_n^{KS}(\mathbf{r}')]^*}{\omega - \varepsilon_n^{KS} + i\eta \times \text{sgn}(\varepsilon_n^{KS} - \mu)}$$

with μ the Fermi energy. The knowledge of the self-energy operator allows to calculate the GW Green’s function and energy levels by replacing the DFT exchange-correlation potential contribution

by the GW self-energy operator calculated at the targeted GW energy, namely:

$$G(\omega) = G^{KS}(\omega) + G^{KS}(\omega) \left[\Sigma^{GW}(\omega) - V_{DFT}^{XC} \right] G(\omega)$$

and for the energy levels:

$$\varepsilon_n^{GW} = \varepsilon_n^{KS} + \langle \phi_n^{KS} | \Sigma^{GW}(\varepsilon_n^{GW}) - V_{DFT}^{XC} | \phi_n^{KS} \rangle$$

Such a scheme, where the self-energy is built from the Kohn-Sham input eigenstates, is labeled the single-shot, or G_0W_0 , approach, as compared to self-consistent techniques where corrected eigenvalues, possibly eigenstates, are reinjected to calculate G and W .

In the fragment GW approach, one assumes that the system is partitioned in subsystems (labeled also fragments or clusters below) with weakly overlapping wavefunctions. In that limit, the independent-electron susceptibility χ_0 (Eq. 3) has hardly any contribution from orbitals ϕ_n and ϕ_m belonging to different fragments. The susceptibility χ_0 is then diagonal by blocks, each block built from the susceptibility of one fragment in the isolated (gas phase) limit. This represents a considerable saving since in the fragment limit the cost of calculating the overall χ_0 does not grow quartically with system size, but only linearly. If the fragments are identical, just translations of the same cluster with identical susceptibility blocks, calculating the overall χ_0 is independent of the system size. Such a fragment GW approach was used in particular in the study of π -conjugated organic crystals, with weak interactions between molecular units, [61, 62] nanotube bundles [63] or layered 2D systems bound by weak van der Waals interactions, defining the field of 2D-genomics [64–67]. Further, such a partitioning of the independent-electron susceptibility served as the basis for combining the GW and Bethe-Salpeter [68–70] formalisms with semi-empirical continuous or discrete models of polarizable environments [71–75].

In the present study, we not only neglect the wavefunction overlap between neighboring layers, as already done in several studies [64–67], but we further fragment individual monolayers in domains. This is done by “reconstructing” monolayers by patching h -BN clusters as symbolically represented in Fig. 1. Writing the independent-electron susceptibility as a sum over fragments (indexed by I) in matrix notations, with ($I = 0$) the defected fragment (or cluster), one writes:

$$\begin{aligned} \chi_0(\mathbf{r}, \mathbf{r}'; \omega) &= \chi_0^{(I=0)}(\mathbf{r}, \mathbf{r}'; \omega) + \sum_{I>0} \chi_0^{(I)}(\mathbf{r}, \mathbf{r}'; \omega) \\ &= \chi_0^{(defect)}(\mathbf{r}, \mathbf{r}'; \omega) + \sum_{I>0} \chi_0^{(pristine)}(\mathbf{r} - \mathbf{R}_I, \mathbf{r}' - \mathbf{R}_I; \omega) \end{aligned}$$

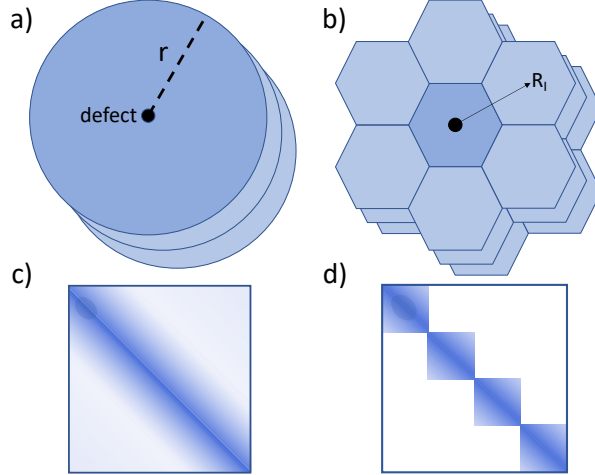


FIG. 1. Symbolic representation of a finite-size multilayers system. The defect is represented here by the black dot at the center of the surface layer or central fragment in darker blue. In (a), convergence to the infinite-layer limit can be achieved by increasing the radius r with a large computational cost increase, while in (b) the same limit is reached by adding shells of first, second, etc. nearest neighbor domains, namely undefected fragments translated by a set of $\{\mathbf{R}_l\}$ vectors. The corresponding independent-electron susceptibility matrices are represented in c) and d) respectively.

where $\chi_0^{(pristine)}$ is the susceptibility of an undefected (pristine) h -BN cluster and the $\{\mathbf{R}_l\}$ are the translations needed to reconstruct all layers with h -BN fragments. Such an approach only requires the susceptibility $\chi_0^{(defect)}(\mathbf{r}, \mathbf{r}'; \omega)$ of an isolated defected h -BN cluster and the susceptibility $\chi_0^{(pristine)}(\mathbf{r}, \mathbf{r}'; \omega)$ of an undefected h -BN cluster that will be “translated” to fill up the full system $\chi_0(\mathbf{r}, \mathbf{r}'; \omega)$ matrix (see Fig. 1d). For the defected layer, the central fragment contains the defect, surrounded by shells of first, second, etc. nearest-neighbor pristine h -BN clusters. In practice, each layer contains up to 4-th neighbor fragments, amounting to 57 clusters containing typically 86 to 138 atoms each, reaching lateral sizes large enough to allow extrapolation to the infinite layer size limit for a given number of layers. The accuracy of this scheme will be carefully validated below.

While the non-interacting χ_0 blocks are decoupled, it is important to keep in mind that all fragments interact in the construction of the screened Coulomb potential W . With the notations defined above, the Dyson-like equation 2 allows to write the screened Coulomb potential in block notations as:

$$W = v + v \left[\sum_I \chi_0^I + \sum_{IJ} \chi_0^I v_{IJ} \chi_0^J + \sum_{IJK} \chi_0^I v_{IJ} \chi_0^J v_{JK} \chi_0^K + \dots \right] v$$

where the v_{IJ} are the bare Coulomb matrix elements between fragments (I) and (J). As such, the

screened Coulomb potential includes all order interactions between fragments via the bare Coulomb potential.

We conclude by noting that while the cost of building the independent-electron susceptibility, the most expensive step in a GW calculation, is dramatically reduced in the fragment approach, inverting the Dyson equation for W remains to be done (Eq. 2), with a cubic scaling cost with system size. However, systems with hundreds of domains, adding up to thousands of atoms, can be treated fully *ab initio* as discussed here below.

B. The static COHSEX approximation for environmental screening

To further reduce the cost of inverting the Dyson equation for $W(\omega)$ at each frequency, we further explore the merit of a popular approximation to the full GW dynamical self-energy operator labelled the static Coulomb-hole (COH) plus screened exchange (SEX) approximation. The COHSEX terminology describes an exact partitioning of the self-energy, gathering in the SEX/COH terms the contributions from the poles of G/W [76–78]. The static approximation takes to zero all energy differences ($\varepsilon_n - \omega$) in the COHSEX terms, where ε_n covers the spectrum of electronic energy levels and ω is the frequency at which the self-energy is to be calculated, yielding:

$$\begin{aligned}\Sigma_{static}^{SEX}(\mathbf{r}, \mathbf{r}'; 0) &= - \sum_n^{occ} \phi_n(\mathbf{r})\phi_n^*(\mathbf{r}')W(\mathbf{r}, \mathbf{r}'; \omega = 0) \\ \Sigma_{static}^{COH}(\mathbf{r}, \mathbf{r}'; 0) &= \frac{1}{2} \sum_n \phi_n(\mathbf{r})\phi_n^*(\mathbf{r}')(W - v)(\mathbf{r}, \mathbf{r}'; 0) \\ &= \frac{1}{2} \delta(\mathbf{r} - \mathbf{r}')(W - v)(\mathbf{r}, \mathbf{r}'; \omega = 0).\end{aligned}$$

This static approximation offers the advantage that the screened Coulomb potential only needs to be calculated at the low-frequency limit ($\omega \rightarrow 0$), greatly reducing computer cost. In the present analytic continuation implementation of GW [79, 80], for which the susceptibility needs to be calculated at typically 12 frequencies along the imaginary axis, the static COHSEX approximation is thus an order-of-magnitude cheaper than the full GW calculation.

Such an approximation was shown to yield significantly too large gaps [77] but has been central to most studies implementing the fragment many-body techniques [62, 81] or the combination of many-body techniques with models of dielectric environment [73, 74]. In such studies, environmental corrections are calculated within the static COHSEX approximation in the form of a difference,

namely that of the static COHSEX values of an energy level with and without the environment. In practice, this means that the GW energy levels for a defected fragment surrounded (embedded) by undefected h -BN flakes is calculated as:

$$\varepsilon_n^{eGW} \simeq \varepsilon_n^{gGW} + (\varepsilon_n^{eCOHSEX} - \varepsilon_n^{gCOHSEX})$$

where eGW and $eCOHSEX$ mean embedded GW and COHSEX calculations, while gGW and $gCOHSEX$ point to gas phase, namely isolated defected fragment calculations.

The difference $\Delta_n^{GW} = (\varepsilon_n^{eGW} - \varepsilon_n^{gGW})$ and its approximation $\Delta_n^{COHSEX} = (\varepsilon_n^{eCOHSEX} - \varepsilon_n^{gCOHSEX})$ that characterizes the evolution of electronic energy levels from the monolayer to the multilayer cases (few-layers, surface, bulk) is the main targeted observable of the present study. Such an energy shift may be decomposed into two contributions : (a) the shift of the Kohn-Sham energies $\Delta_n^{KS} = (\varepsilon_n^{eKS} - \varepsilon_n^{gKS})$ and (b) the shift due to screening effects at the ΔGW or $\Delta COHSEX$ level. The quantity Δ_n^{KS} accounts for hybridization, confinement, or electrostatic effects in the ground-state, while the second occurs as a response to an electronic excitation (e.g. photoemission) on the defect. We will label polarization energy this second contribution that can be defined as the difference $P_n = \Delta_n^{GW} - \Delta_n^{KS}$. While Δ_n^{KS} can shift up or down energy levels, the second effect always stabilizes holes and electrons, namely pushing occupied levels towards the vacuum level, while on the contrary empty levels go down in energy.

Physically, the use of the static COHSEX approximation implies the neglect of the frequency dependence of the dielectric response, assuming that the environment reacts instantaneously to an excitation in the central system of interest, with the susceptibility obtained in the low-frequency limit. This approximation may be questionable in cases where the gap in the environment electronic excitation spectrum is not clearly larger than that of the central object of interest. We will thus for validation compare ΔGW and static $\Delta COHSEX$ polarization energies.

C. Technical details

Our DFT calculations are performed with the ORCA code [82] that is used to obtain relaxed geometries and generate the Kohn-Sham eigenstates used as an input for many-body GW corrections. Such many-body calculations are performed with the BeDefT (Beyond-DFT) package [79, 80], an evolution of the FIESTA code [83–86], that implements the GW formalism within a Gaussian basis formalism. The dynamical self-energy is obtained using an improved analytic continuation scheme

[79, 80] that does not require any plasmon-pole approximation. All occupied, including core states, and unoccupied energy levels are included in the construction of the susceptibility and self-energy. Coulomb integrals are calculated using standard Coulomb-fitting resolution of the identity [87–89]. At that stage, we emphasize that the present all-electron finite-size calculations with Gaussian basis sets, not relying on the Bloch theorem nor on the use of pseudopotentials, provide energy levels directly referenced to the vacuum level.

Structural relaxations are performed at the triple-zeta plus polarization 6-311G(d) level [90]. We adopt the same basis for the calculation of energy differences at the GW and static COHSEX level. While absolute GW energies are not converged with such a basis set, energy differences between the defected monolayer and corresponding multilayer systems are very well captured. Such energy differences involve long-range polarization effects that converge very quickly with basis size, as further demonstrated below in our discussion on the basis-set dependence of the fragments dipolar response.

Our GW calculations are performed at the non-self consistent G_0W_0 level starting with a PBEh(α) functional [91] with 40% of exact exchange ($\alpha = 0.4$). In the process of calculating polarization energies, input Kohn-Sham eigenstates enter indirectly through the construction of the χ_0 Kohn-Sham independent-electrons susceptibility. Since we are interested in exploring the impact of the dielectric response of added layers on the defect, we adopt an α value close to the optimal one ($\alpha = 0.409$) found in Ref. 25 for reproducing the monolayer long-range dielectric properties in an optimally tuned-functional approach. We emphasize however that Kohn-Sham eigenstates are used in the present case as an input starting guess to build the dielectric function and the GW self-energy. This GW correction dramatically reduces the impact of the chosen DFT functional on the final quasiparticle energies. Anticipating on the upcoming results, the shift in energy for the carbon-dimer defect levels from the monolayer to the h -BN bulk changes by no more than 10% taking PBE Kohn-Sham eigenstates instead of PBEh(0.4) ones as starting points, even though the related Kohn-Sham gaps differ by ~ 3 eV (monolayer limit).

We now address an important aspect of our calculations pertaining to the idea of multipole expansions. In the standard Coulomb-fitting resolution-of-the-identity (RI-V) technique we adopt [87–89], orbital products $\phi_m(\mathbf{r})\phi_n(\mathbf{r})$ appearing in the construction of the independent electron

susceptibility (Eq. 3) are expressed over an auxiliary basis $\{P_\mu\}$ of Gaussian orbitals:

$$\begin{aligned}\phi_m(\mathbf{r})\phi_n(\mathbf{r}) &= \sum_{\mu} C_{\mu}^{nm} P_{\mu}(\mathbf{r}) \\ C_{\mu}^{nm} &\stackrel{RI-V}{=} \sum_{\nu} [V^{-1}]_{\mu\nu} (\phi_m\phi_n|P_{\nu})\end{aligned}$$

where $V_{\mu\nu}$ are Coulomb matrix elements in the auxiliary basis and $(\cdot|\cdot)$ denotes a Coulomb integral. Such $\phi_m(\mathbf{r})\phi_n(\mathbf{r})$ products, and their representative auxiliary basis set, enter in the description of the charge rearrangements induced by a perturbation in the system. In finite size systems, molecular orbitals can be taken to be real. The independent-electron susceptibility is calculated in the auxiliary basis with:

$$\begin{aligned}\chi_0(\mathbf{r}, \mathbf{r}'; i\omega) &= \sum_{\mu\nu} [\chi_0(i\omega)]_{\mu\nu} P_{\mu}(\mathbf{r}) P_{\nu}(\mathbf{r}') \\ [\chi_0(i\omega)]_{\mu\nu} &= \sum_{mn} \frac{(f_m - f_n) C_{\mu}^{nm} C_{\nu}^{nm}}{i\omega - (\varepsilon_m - \varepsilon_n)}\end{aligned}$$

Such auxiliary basis sets, that span the ‘‘product-space’’ of Kohn-Sham orbitals, have been optimized for each standard Gaussian Kohn-Sham basis and we use the universal Coulomb fitting auxiliary basis [92] in conjunction with the 6-311G(d) basis set. It is in such an auxiliary basis representation that the Dyson equation for the screened Coulomb potential W is inverted or, equivalently, the interacting susceptibility χ :

$$\chi(\mathbf{r}, \mathbf{r}'; \omega) = \chi_0(\mathbf{r}, \mathbf{r}'; \omega) + \int d\mathbf{r}_1 d\mathbf{r}_2 \chi_0(\mathbf{r}, \mathbf{r}_1; \omega) v(\mathbf{r}_1, \mathbf{r}_2) \chi(\mathbf{r}_2, \mathbf{r}'; \omega)$$

Reducing the size of the auxiliary basis can quickly degrade the quality of correlated calculations. We have observed however that the polarizability tensor $\{\alpha_{ij}\}$ of a given fragment:

$$\alpha_{ij}^{(I)} = - \int d\mathbf{r} d\mathbf{r}' r_i \cdot \chi^{(I)}(\mathbf{r}, \mathbf{r}'; \omega) \cdot r'_j$$

with $\chi^{(I)}$ the interacting susceptibility of fragment (I) in the gas phase, is hardly affected by reducing significantly the auxiliary basis set. In the case of the h -BN fragments considered in this study, removing the (d, f, g)-character orbitals and the core (s, p) ones from the auxiliary $\{P_{\mu}\}$ basis set hardly changes the fragment dipolar polarizability, with error well below the percent. We use such reduced auxiliary basis sets to expand the microscopic susceptibility $\chi_0^{(I)}$ of fragments that are beyond the first-nearest-neighbors of the central defected fragment of interest. As a result, the calculated polarization energies from the monolayer to the multilayer cases do not change by more

than a very few meVs. We interpret this favorable behavior by emphasizing that for long-range interactions, induced dipoles are the major contribution to the reaction field and polarization energy. As such, an approximation that preserves the calculated dipolar tensor of remote fragments may be very accurate as we observe. We do not attempt to reduce the basis of nearest neighbor fragments.

D. Geometries

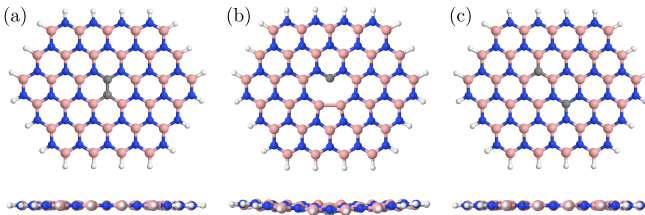


FIG. 2. Ball-and-stick representation of the (a) carbon-dimer (CC) defect, (b) the $C_B V_N$ defect and (c) the carbon-dimer defect in the 4-th nearest neighbor configuration labeled $CC-\sqrt{7}$ [93]. Defects are located at the center of a BN86 flake (or fragment). Edge atoms are passivated by hydrogen. The CC defect in the BN138, BN202 and BN278 fragments are reproduced in the SM [94]. In the $C_B V_N$ defect, the carbon atom stands ~ 0.5 Å below the average plane defining the defected layer (see text).

We study *h*-BN clusters containing 86, 138, 202 and 278 atoms with passivating hydrogens at the edge. Such systems will be named BN86, BN138, etc. In the case of defected structures, the defect is located at the center of the cluster. We represent in Fig. 2(a,b,c) the paradigmatic neutral carbon-dimer (labeled CC) and $C_B V_N$ defects, together with the so-called $CC-\sqrt{7}$ carbon-dimer variant [93]. In the following, we will use e.g. the notation $CC@BN86$ for a CC defect at the center of a BN86 flake or cluster. The carbon-dimer defect has been proposed [29, 36] to be a likely candidate for the frequently observed 4.1 eV emission line, while the $C_B V_N$ defect has been associated with the ~ 2 eV emission line [33, 95]. The $CC-\sqrt{7}$ carbon-dimer defect, with carbon atoms in 4-th nearest neighbor position, is less stable than the standard (nearest-neighbor) CC carbon-dimer defect [93]. However it exhibits a larger spatial extension and a gap significantly smaller (by ~ 2.2 eV at the *GW* level for the monolayer) than the standard carbon-dimer defect, allowing to show below that polarization (screening) effects are nearly independent of the geometrical and electronic properties of the defect of interest. All structures are relaxed at the PBE0 6-311G(d) level.

Except for the non-planar $C_B V_N$ defect, we do not attempt to relax multilayer systems. In the

dilute limit, the energetics around the defect is not expected to govern the stacking properties of the h -BN layers. As a test, in the case of the carbon-dimer defect located in a BN86 fragment, we prepare a bilayer by adding an undefected BN86 fragment in a AA' stacking geometry with the experimental 3.33 Å interlayer spacing [96, 97]. Structural relaxation including D3 dispersion forces [98] preserves the AA' stacking geometry, with a slightly reduced 3.25 Å interlayer spacing in the relaxed bilayer. As such, even in the rather high-doping limit, planarity and stacking are preserved for the carbon-dimer defects. In what follows, we will thus relax individually the layers and stack them in an AA' fashion with the experimental 3.33 Å interlayer spacing.

The case of the $C_B V_N$ defect is more complicated since the relaxation of a single-layer defected fragment leads to a highly non-planar system (see SM [94]). This is due presumably to the tensile strain induced by forming a B-B bond across the missing N atom. However, adding a second undefected fragment in AA' stacking and relaxing with D3 dispersion corrections allows to dramatically restore planarity thanks to layer-layer interaction. Nevertheless, the C-atom goes towards the neighbouring layer with an out-of-plane deviation of about 0.55 Å. The same result is obtained in a trilayer system where the defect is sandwiched between two undefected layers, the C atoms remaining 0.52 Å out of plane despite the restored symmetry of having one layer on each side of the defect. In what follows, we thus adopt the bilayer or trilayer geometry, for studying the surface and bulk limits, and add subsequent layers in an AA' stacking geometry and a 3.33 Å distance with respect to the nearest undefected layer.

III. FRAGMENTING THE MONOLAYER

In a previous study [36], the monolayer CC dimer defect was studied using the GW and Bethe-Salpeter formalisms within a finite-size cluster approach, following the variation of the quasiparticle gap and optical excitation energies as a function of cluster size. It was shown in particular that the defect electronic energy levels converge very slowly with system size following a $1/R^2$ scaling law, with R the average radius of the defected h -BN cluster considered. Such a scaling law was shown to originate from long-range polarization, or screening, effects in a 2D system [99]. To reach such an asymptotic regime, allowing to extrapolate to the infinite size limit, GW calculations on systems with increasing sizes well above two hundred atoms had to be considered. Such results are reproduced in Fig. 3(a) at the present $G_0W_0@PBEh(0.4)$ (red circles) and static COHSEX@PBEh(0.4) (black circles) levels. The evolution of the gap of a CC defect at the center

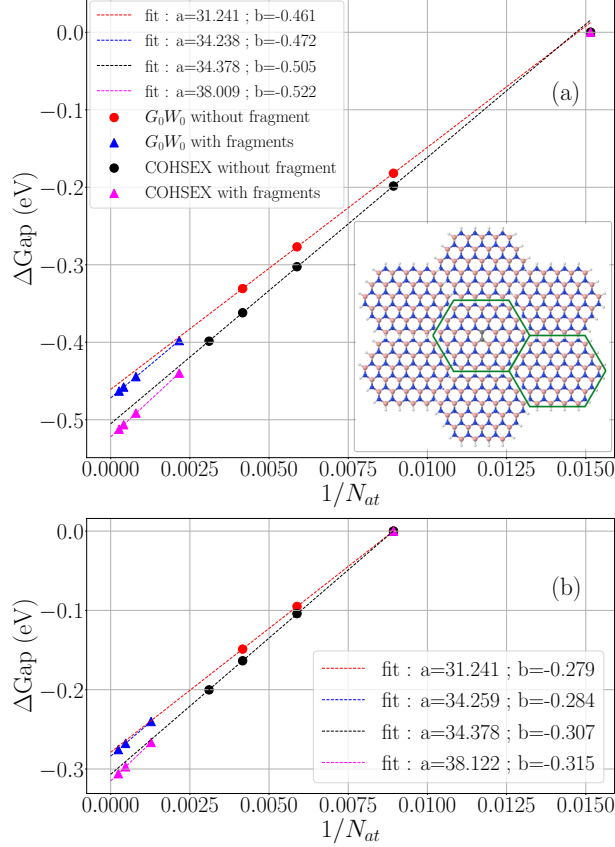


FIG. 3. Evolution of the gap between the occupied and unoccupied CC defect energy levels with respect to (a) the CC@BN86 and (b) the CC@BN138 cluster gaps as a function of $1/N_{at}$. The red (black) dots are full G_0W_0 (COHSEX) calculations for the CC@BN138, CC@BN202 and CC@BN278 clusters. The blue (pink) up-triangles represent fragment G_0W_0 (COHSEX) calculations for (a) a central defected CC@BN86 cluster surrounded by up to four shells of undefected BN86 fragments, and (b) a central defected CC@BN138 cluster surrounded by up to three shells of undefected BN138 fragments. Dashed lines are $[a/N_{at} + b]$ fits. (Inset) Symbolic representation of the fragment approach for building the susceptibility. The central CC@BN86 defected fragment is surrounded by undefected pristine BN86 first-nearest-neighbor fragments. Larger systems can be reconstructed by adding 2nd, 3rd, etc. neighbor fragments (not represented here).

of BN138, BN202 and BN278 flakes (see geometries in SM [94]) are given, taking as a reference the smallest CC@BN86 system. The dashed lines with corresponding colors are a $(1/N_{at})$ linear fit of the data, with N_{at} the number of N/B atoms that is proportional to the squared radius of the flake. We excluded the smaller CC@BN86 system for these fits to obtain an improved linear behavior, indicating that large systems must be considered to be in the limit where the fit is accurate.

The significant evolution of the gap is the signature of the influence of enhanced screening by

additional B/N atoms. In the asymptotic infinite monolayer size limit, the defect gap is closing by 0.46 eV (G_0W_0) or 0.51 eV (static COHSEX) as compared to the smaller CC@BN86 system. A small contribution from the closing of the gap originates from the evolution of the Kohn-Sham gap that can be fitted with a $[1.87/N_{at} - 0.05]$ eV law. This change in gap at the DFT level is an order of magnitude smaller than the evolution at the G_0W_0 level, indicating that long-range polarization effects are not captured at the Kohn-Sham DFT level. The closing of the gap due to polarization only, subtracting the ground-state Kohn-Sham contribution, amounts to $(P_e - P_h) = 0.41$ eV at the GW level and originates both from the stabilization of the defect occupied level ($P_h=0.20$ eV) and of the unoccupied one ($P_e=-0.21$ eV), where the subscript h and e stand for hole and electron, respectively. We show now that the same results can be obtained by fragmenting the monolayer in domains reproducing the same screening, or polarization, effects on the central defect, but at a dramatically reduced cost allowing to reach much larger system sizes.

To rationalize this strategy, we plot in Fig. 4 the (static) polarizabilities of the pristine (undefected) BN58, BN86, BN138, BN202 and BN278 flakes in the random phase approximation (RPA). It is such an approximation that is used to build the screened Coulomb potential W in standard GW calculations (Eq. 2). Such results show that the polarizability principal components follow accurately a linear relation with respect to the number of B/N atoms. As such, one can define a polarizability-per-atom that is independent of the size of the considered cluster. We believe that such a behaviour is characteristic of insulating systems where charges cannot be displaced from one side of the system to another, and polarization proceeds rather by the creation of local dipoles.

The consequence of such a behaviour is that the effect on the central defect of polarizing a B/N atom located in an infinite monolayer, or at the same distance from the defect but in a finite size cluster, are very similar. Such a finding allows to set up a fully *ab initio* embedding scheme, with a central defected fragment embedded in rings of first, second, third, etc. undefected neighbor fragments (see Inset Fig. 3a) reproducing the effect of a continuous layer at a dramatically reduced cost. As emphasized in the Methodology section, instead of calculating the independent-electron susceptibility χ_0 of a system with increasing size, with a quartic scaling evolution in terms of the number of operations to perform, this susceptibility matrix can be calculated fragment by fragment, in a block diagonal fashion.

To further confirm the preservation of long-range screening upon fragmenting the monolayer, we plot in Fig. 5 the ratio of the statically screened Coulomb potential $W(\mathbf{r}, \mathbf{r}'; \omega = 0)$ over the bare Coulomb potential V , with W obtained from Eq. 2 and the susceptibility χ_0 built in a block-diagonal

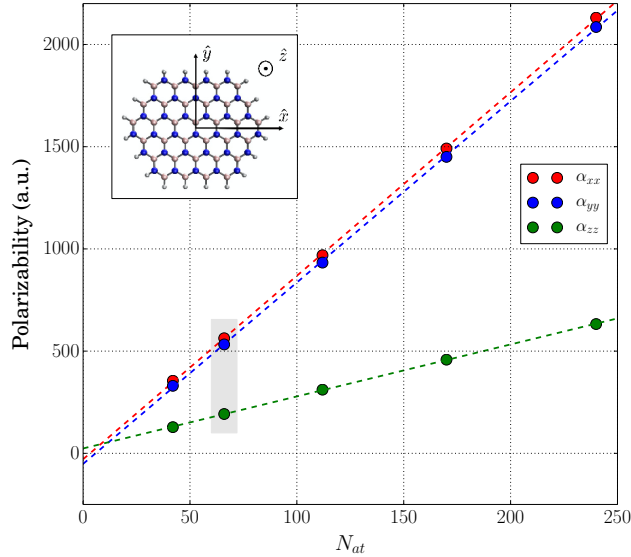


FIG. 4. Evolution of the RPA static polarizability (in atomic units) of pristine *h*-BN clusters with increasing number of B/N atoms. The three principal axes polarizabilities are given. The smallest contribution indicates the out-of-plane polarizability. The shaded data indicates the BN86 flake (see Inset) used to fragment/reconstruct extended monolayers in the following.

fashion from gas phase χ_0^{defect} and $\chi_0^{pristine}$ fragment susceptibilities. The \mathbf{r} point is fixed to the CC bond center while \mathbf{r}' varies radially in a specific direction that goes close to H atoms when reforming the monolayer with BN86 fragments, and across H atoms when reconstructing the monolayer with larger BN138 fragments (see horizontal black dashed lines). The W/V ratio is very similar in both cases, with small differences when crossing or coming close to H atoms. In the vicinity of the CC bond, where the defect states are localized, the W/V ratio for the two systems are indistinguishable. As such, changing the fragments size, that is changing the ratio of H atoms to B/N ones, hardly affects the screening properties. As expected for a 2D system, the W/V ratio converges to unity in the long range limit [54, 100–102], at odds with the $1/\epsilon_M$ limit in 3D systems, where ϵ_M is the macroscopic dielectric constant. This is a clear indication that long-range screening properties in 2D or 3D systems cannot be reproduced within DFT by the same functional. A plot of the W/V ratio in several directions is provided in the SM [94].

We now compare the G_0W_0 and COHSEX calculations performed for the CC@BNX systems, with X varying from 86 to 278, to the fragment approach where the monolayer is fragmented in BN86 defected (center) and undefected fragments with interacting polarizabilities. Since the

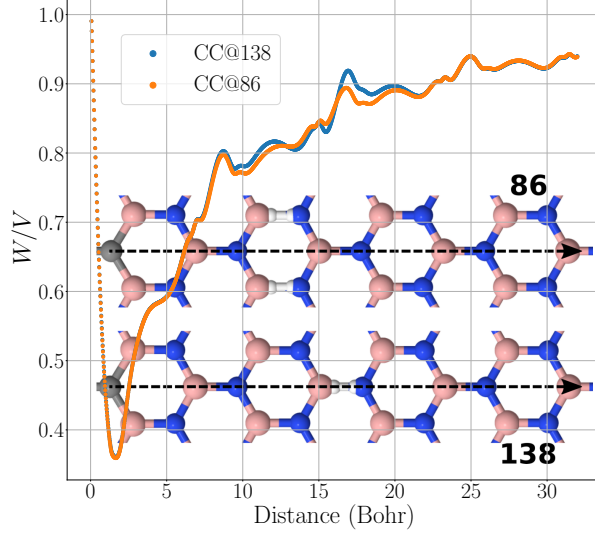


FIG. 5. Ratio of the statically screened Coulomb potential $W(\mathbf{r}; \mathbf{r}'; \omega = 0)$ divided by the bare Coulomb potential V with \mathbf{r} fixed at the center of the CC bond and \mathbf{r}' varying along the direction indicated by the horizontal black dashed lines. The case of a defected monolayer reconstructed with BN86 fragments (orange plot) or larger BN138 fragments (blue plot) are compared.

fragment approach can only account for polarization effects at the $GW/COHSEX$ level, the small $[1.87/N_{at} - 0.05]$ eV (see above) evolution of the Kohn-Sham gap with system size beyond the 86-atoms system is added perturbatively to the polarization correction. As emphasized above, such a perturbative approach is justified by the order-of-magnitude difference between gap changes at the Kohn-Sham and many-body levels. As a result, extrapolations from the full (un-fragmented) calculations (red and black dotted lines) and from the much cheaper fragment approach (up-triangles and corresponding fit) differ by no more than 11 meV (17 meV) in the G_0W_0 (COHSEX) calculations. As can be seen from the graph, the system including the 4-th shell of nearest neighbor fragments, amounting to 57 flakes of 86 atoms each, (see e.g. blue up-triangle at the G_0W_0 level) is already very close to the asymptotic infinite limit.

The very same exercise can be performed by reconstructing the infinite monolayer with larger BN138 fragments. Adopting larger fragments allows reducing the possible effects of edge H atoms polarizability. The results are represented in Fig. 3(b). Since we start from a larger system, the infinite size correction is smaller. The extrapolated value using the fragment approach falls within 5 meV (8 meV) of the extrapolated value obtained without any fragment approximation at the G_0W_0 (COHSEX) level. As such, fragmenting the monolayer with small BN86 units or larger 138 units

leads to very close results, confirming that edge effects (e.g. hydrogen polarization) are negligible.

For further validation, we explored even larger systems using an efficient classical induced-dipole model of polarizable points [99, 103] with site polarizabilities fitted to reproduce the results of Fig. 4. Such a microelectrostatic model allows to reach systems more than one order of magnitude larger than the one we can afford at the *ab initio* level with the fragment approach. The outcome of these model calculations is that extrapolating the evolution of the gap to the infinite monolayer on the basis of data acquired with much larger systems does not change by more than a meV the extrapolated value obtained with systems of the size we study *ab initio* in the present fragments scheme. This is reported in more details in the SM [94].

Coming back to the distinction between static and dynamical *GW* calculations, we observe at that stage that the static COHSEX approximation leads to polarization energies that are overestimated by about 10% as compared to G_0W_0 calculations. Namely, the static COHSEX approximation slightly overestimates the closing of the gap due to enhanced dielectric screening.

IV. FROM THE MONOLAYER TO MULTILAYERS

We now study the effect of layering on the defect energy levels, considering first the carbon-dimer defect. We start our exploration by providing in Fig. 6 the evolution of the defect G_0W_0 (red stars) and COHSEX (blue stars) gaps from the monolayer to n -layer systems in a 86-atoms finite size layered geometry. Namely, we here do not stack infinite layers but create a "cylinder" of stacked 86-atoms flakes, with a surface defected CC@BN86 cluster deposited on top of undefected BN86 clusters in an AA' stacking fashion with 3.33 Å separation between layers (see schematic Inset Fig. 6). We start with full G_0W_0 and COHSEX calculations, without any fragment approximation, stopping at 5-layers, representing already 430 atoms.

As expected, interlayer screening reduces the gap associated with the defect. At the G_0W_0 level in this 86-atoms stack geometry, the gap closes by as much as 0.4 eV upon adding a second layer, 0.49 eV with a third layer, etc. Such a correction can be compared to the 0.106 eV closing of the gap at the Kohn-Sham level originating from the addition of a second layer, the difference between the pentalayer and the bilayer being reduced to 4 meV. This illustrates again that Kohn-Sham DFT cannot reproduce long-range screening unless a strategy is adopted to readjust the functional for each number of layers in order to mimic increased screening with increasing number of layers. [25] Concerning many-body approaches, we observe again that the static COHSEX approximation

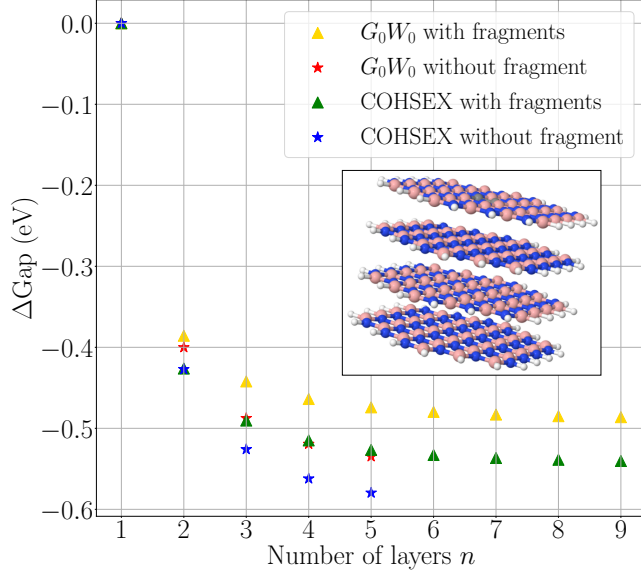


FIG. 6. Evolution as a function of the number of layers of the defect gap of a defected CC@BN86 cluster located at the surface of a stack of BN86 undefected fragments in an AA' geometry. The reference is taken to be the monolayer CC@BN86 fragment. Full G_0W_0 (red stars) and COHSEX (blue stars) are compared to fragment G_0W_0 (yellow up-triangles) and COHSEX (green up-triangles). The wording “fragments” means here a decoupling of layer wavefunctions. Inset: Schematic representation of the ($n=4$) system. Energies are in eV.

overestimates the effect of screening, even though the error ranges from 30 to 50 meV, to be compared to the 0.4-0.6 eV total correction, namely an error not larger than 10%.

In a second step, we adopt a fragment approach, namely decoupling the wavefunctions at the Kohn-Sham level between adjacent layers, constructing the independent-electron susceptibility in a block-diagonal fashion from the susceptibility of the isolated layers. Such an approach has been used in several previous studies devoted to exploring the properties of stacked 2D systems (intercalating e.g. h -BN, graphene, dichalcogenides) [64, 67]. As done in the previous Section for reaching the infinite monolayer limit, the small Kohn-Sham shift between monolayer and multilayer systems is added perturbatively to the fragment GW and COHSEX calculations to allow comparison with the full (unfragmented) calculations.

The present decoupling scheme is shown in Fig. 6 to underestimate the impact of screening on the defect gap beyond the bilayer system (compare the yellow up-triangles to the red stars at the G_0W_0 level and the green up-triangles to the blue stars at the COHSEX level). The error is however

of the order of 50 meV at most, to be compared to a total correction of 0.4-0.5 eV. This relatively small error certainly confirms the success of the fragment approach in the 2D-genomics studies.

We further observe that this error is comparable in magnitude with that induced by the static COHSEX approximation, but with an opposite sign. As a result, and up to the 5-layers system, for which full reference G_0W_0 calculations were possible, there is a significant cancellation of errors between the static COHSEX approximation, that overestimates the effect of screening, and the fragment approximation that underestimates it. We conclude from these tests that the fragment plus static COHSEX approximation reproduces with a limited error full G_0W_0 calculations, thanks to a cancellation of error between the static and the fragment approximations. This cancellation reduces the 30-50 meV error associated with each separate approximation to a significantly lower value. While this cancellation is certainly fortuitous, since both errors are of different nature, we adopt this scheme in the following.

We now explore within the fragment static COHSEX scheme the evolution of the correction upon increasing the size of the layers, namely trying to converge towards the stacking of infinite size layers. We first study in Fig. 7(a) the effect of stacking 138-atoms (red squares) and 202-atoms (blue pluses) flakes beyond the 86-atoms (green up triangles) systems studied in Fig. 6. The defect is here again localized on the surface layer. Clearly, as expected, increasing the size of each layer leads to increasing the polarization energy.

Enlarging further the size of each layer becomes prohibitively expensive. We thus adopt the strategy of Section III where we increase the in-plane lateral size by patching undefected BN86-atoms fragments around each CC@BN86 (defected layer) or BN86 (undefected layers) central fragment. Adding first, second, third and fourth nearest neighbor flakes allows reaching much larger layers. These systems are large enough to extrapolate to infinite size layers for each (n) value. This is again carefully checked with the semi-empirical model of polarizable points (see SM [94]). Reaching the asymptotic regime is shown to be more difficult upon increasing the number of layers, suggesting that convergence criteria are related to the aspect ratio of the systems.

The polarization energies extrapolated to the infinite layer size for each (n) value are represented by horizontal black dashed segments. Analytic derivation shows that in the limit of infinite size layers, polarization energies should scale as $(1/n)$ as a function of the number (n) of layers. This is what we observe in Fig. 7 with a fit of the $n=4$ to 7 layers extrapolated values by a $[0.55/n - 0.90]$ eV functional form. Turning now to the bulk case (see Fig. 7b), adding additional layers alternatively on one side and the other of the defected layer, one obtains an asymptotic evolution of the gap

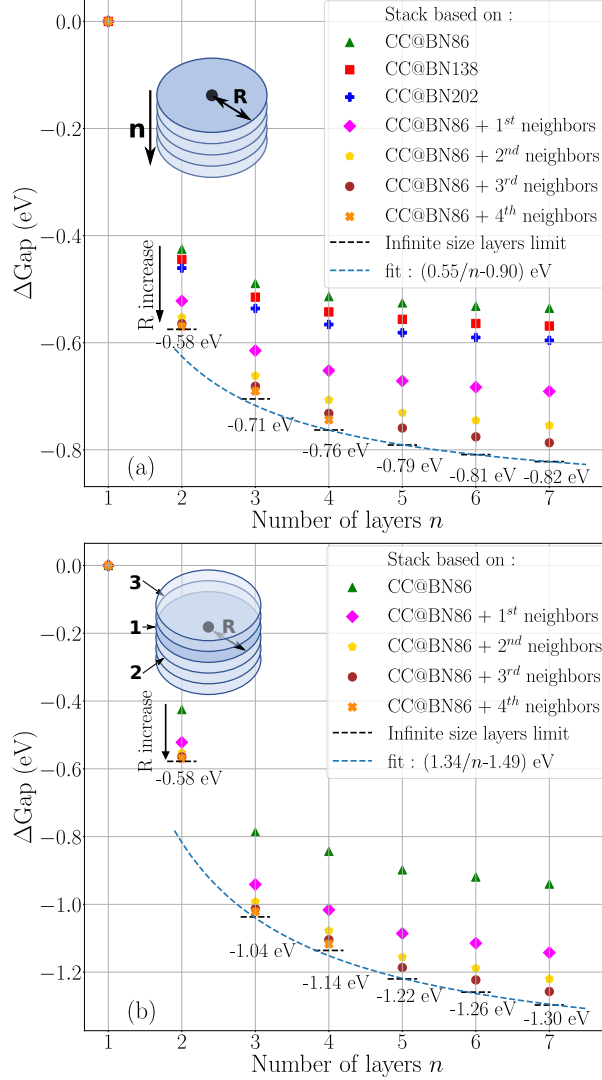


FIG. 7. Evolution of the defect gap (with respect to the monolayer) as a function of the number of layers (n) and the size of each layer. In (a) the defect is on the surface layer, while in (b) it is in the bulk with layers added alternatively on each side of the defect. The horizontal dashed black lines are extrapolations to the infinite layers size for a given (n) value. The extrapolated gap closing value is given underneath. Extrapolated data points can be nicely fitted by a $[0.55/n - 0.90]$ (eV) functional form for the defect at the surface and $[1.34/n - 1.49]$ (eV) for the defect in the bulk. Data obtained at the fragment ΔCOHSEX level.

from the monolayer to the bulk that scales as $[1.34/n - 1.49]$ eV. Even though fitting the $n=5$ to 7 layers data, the functional form yields a gap closing by 1.04 eV and 1.16 eV for $n=3$ and $n=4$, respectively, in close agreement with the 1.04 eV and 1.14 eV explicit values. This indicates that the asymptotic regime is already quite accurate for very few layers. The $n=2$ case, very far

from the asymptotic limit, can be much better estimated by the “surface” fit that yields -0.63 eV, within 0.05 eV of the explicit $\Delta\text{Gap}=-0.58$ eV value. This rapid recovery of the $(1/n)$ asymptotic behavior of the polarization energy with respect to the number of layers was again confirmed with the semi-empirical micro-electrostatic model presented in the SM [94].

As expected, the closing of the gap by 1.49 eV in the bulk limit as compared to the monolayer is significantly larger than the 0.90 eV value found for a defect at the surface. We observe that for $(n=3)$ the polarization energy correction accounts for $\simeq 70\%$ (1.04 eV instead of 1.49 eV) of the $(n \rightarrow \infty)$ limit. This means that the nearest layers contribute significantly to the screening but that the true bulk limit requires additional layers. Using the obtained functional form, 90% of the polarization energy, or closing of the gap, is obtained for 8 additional layers, that is 4 layers on each side of the defected layer. We provide in the SM [94] a study of defects located in a sub-surface and sub-sub-surface layer.

Reproducing for the $C_B V_N$ defect the same study performed here above for the carbon-dimer defect in the bulk limit (see SM [94]), the closing of the gap from the monolayer to the bulk amounts to 1.45 eV, very close to the 1.49 eV value obtained for the CC defects. These values are consistent with the 1.27 eV, 1.31 eV and 1.49 eV gap variations obtained for the C_B , C_N and $C_B V_N$ defects within Kohn-Sham DFT using Koopman’s like conditions to adjust the fraction of exact exchange upon changing the number of layers [25]. Such an agreement is remarkable given that the two techniques are significantly different.

We observe thus that the energy shift from the monolayer to the bulk is very weakly defect-dependent. The Kohn-Sham energy shifts between the monolayer and the multilayer systems is expected to change from one defect to another, depending on the local chemistry (hybridization, ionicity, etc.) Considering e.g. the $C_B V_N$ defect, the PBEh(0.4) Kohn-Sham gap is shown to close by about 60 meV from the monolayer to the 3-layer system on the basis of the stack of BN86 fragments. This value can be compared to the 0.19 eV closing in the carbon-dimer defect case. These two shifts are very different in percentage but small in absolute value. We explore in the following Section the stability of the much larger polarization energy induced by long-range screening from one defect to another.

V. POLARIZATION ENERGIES UNIVERSALITY

We now compare the evolution with layers number of the quasiparticle energy levels for several defects, focusing on the CC carbon-dimer defect in its most stable first-nearest-neighbor conformation and its “CC- $\sqrt{7}$ ” 4th-nearest-neighbor geometry, together with the much studied $C_B V_N$ defect. As discussed above, the evolution of the energy levels can be partitioned into a Kohn-Sham correction and the long-range polarization energies. While the Kohn-Sham correction has been shown to be short-range, involving mainly nearest-neighbor layers interaction, and rather small in magnitude, we now show that the larger polarization energy is very much universal, namely system independent.

We plot in Fig. 8(a) the evolution, from the monolayer to the n -layer case, of the defect occupied level polarization energy (P_h), considering both cases of the defected layer in the bulk or at the surface. In the bulk limit, the polarization energies from one defect to another range from 0.57 eV to 0.61 eV, namely a variation around the mean value of about 3%. Further, the prefactors governing the $(1/n)$ evolution are remarkably close, comparing the evolution to the bulk limit and separately the evolution to the surface limit. The $C_B V_N$ defect is associated with the largest polarization energy. We attribute this to the $C_B V_N$ geometry with the carbon atom coming closer to its neighbor layer by ~ 0.5 Å, inducing a larger reaction field from this layer. The two other carbon-dimer defects are planar and, even though showing different in-plane extension and electronic properties, lead to very similar polarization energies.

To further analyze the small differences from one defect to another, we provide in Fig. 8(b) the evolution of the polarization energy for the defect at the surface taking the bilayer system as reference, namely removing the evolution from the monolayer to the bilayer. Clearly, the various defects are characterized by residual polarization energies that are now within a very few meVs. In the case of the bulk, we reproduce the same exercise in Fig. 8(c) but starting from the 3-layer case (one layer on each side of the defected one). Again, the evolution beyond the nearest-neighbor layers is very much defect independent. Such results confirm that the small differences observed in Fig. 8(a) between defects originate mainly from the response of the nearest-neighbour layers, the response of other layers being nearly completely independent of the defect chemical nature.

The present 0.57 eV to 0.61 eV evolution from the monolayer to the bulk of the defects occupied level are consistent with the ≈ 0.6 eV stabilization energy of charged defects from the monolayer to the bulk as obtained in DFT total energy calculations [30]. In this previous study, the h -BN

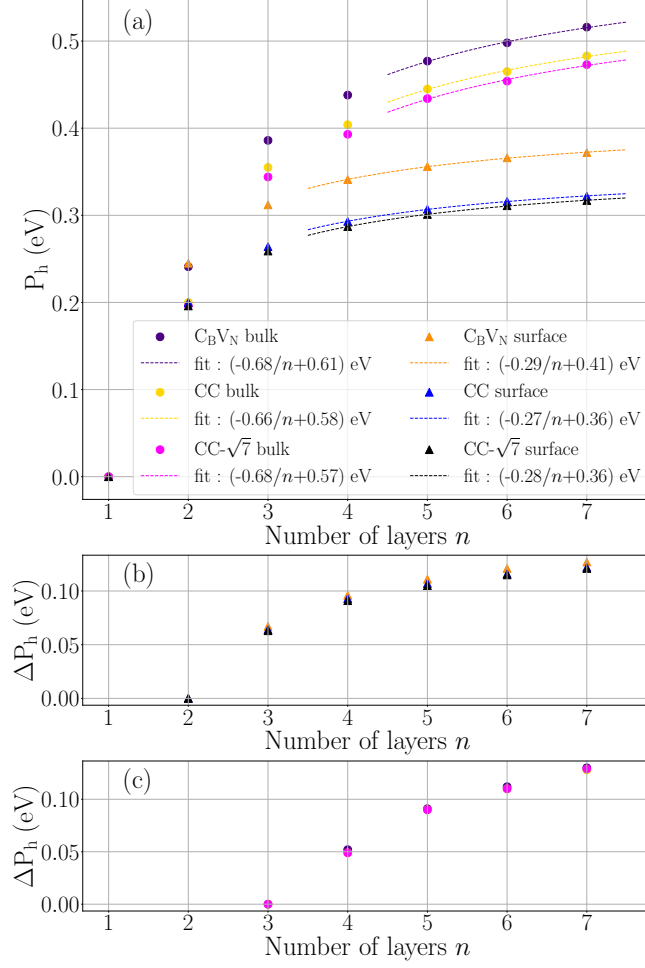


FIG. 8. Polarization energy as a function of the number of layers for the CC , $CC-\sqrt{7}$ and $C_B V_N$ defect-associated occupied level in the surface and bulk limits. In (a) the polarization energy P_h is taken with respect to the monolayer, while in (b) it is taken with respect to the bilayer for surface defects and in (c) with respect to the trilayer (one layer on each side of the defected layer) for the bulk ones. The asymptotic fits are provided.

substrate was replaced by a continuum model of dielectric function accounted for in the Poisson equation used to set up the Hartree potential. It is worth restating here by comparison that the GW formalism accounts for polarization contributions to electronic energy levels, not ground-state total energies as in Ref. 30. Performing the same GW calculations for charged defects would require accounting for long-range screening effects both in the ground and excited states. This stands beyond the scope of the present paper.

We close this section by concluding that polarization energies, originating from environmental screening, are very much universal. Namely, they depend on the host dielectric properties and

on the defect location (surface or bulk), but hardly on the defect chemical nature. Indeed, even though the studied defects showed different chemical composition and band gap, variations of the polarization energies from the monolayer to the bulk are within a very few % of their mean value, and in practice even smaller if the defects do not break the planarity of the defected layer. To better rationalize this universal behavior, we emphasize that the surrounding medium reacts to a localized added charge of which the exact spatial distribution, defect and level dependent, only affects its environment through higher order (dipolar, quadrupolar, etc.) contributions.

The small observed differences originate nearly entirely from the effect of the nearest-neighbor layers. Further, the universal $(1/n)$ long-range behavior, with n the number of layers, starts being valid for a very small number of added layers. In practice, this really means that while Kohn-Sham calculations may have to be performed for a specific defect in the bilayer and trilayer geometries to capture short-range ground-state crystal field and hybridization effects, long-range polarization effects beyond the monolayer case can be accurately accounted for on the basis of the simple scaling laws provided in this paper. As such, expensive *GW* calculations beyond the monolayer limit can be spared when exploring a large zoology of defects in their neutral state.

VI. DEFECT LEVELS WITH RESPECT TO BORON-NITRIDE VALENCE BAND EDGE

All-electron finite-size Gaussian basis sets calculations provide energy levels directly related to the vacuum level. Locating defect levels with respect to the host semiconductor band edge may also be an important issue when it comes to discuss e.g. the evolution with the number of layers of the stability of defect charged states [30]. Contrary to localized states, addressing the energy of extended Bloch states from a finite size cluster calculation is a difficult task as compared to periodic boundary calculations. The flakes to be considered for extrapolating to infinity are much larger than a standard unit cell of the pristine semiconductor, and the physical interpretation in terms of k -points is lost. However, the calculations performed above allow in fact discussing the evolution of defect energy levels with respect to the h -BN valence band edge.

In our defected flake calculations, the levels lying below the defect occupied level are clearly delocalized h -BN states. As such, the scheme presented here above can be used as well to extrapolate to the bulk limit not only the defects localized states, but further the highest occupied h -BN states representative of the h -BN top of the valence band. The results are represented in Fig. 9 which reports the bulk polarization energy, as compared to the monolayer, for a large set of states around

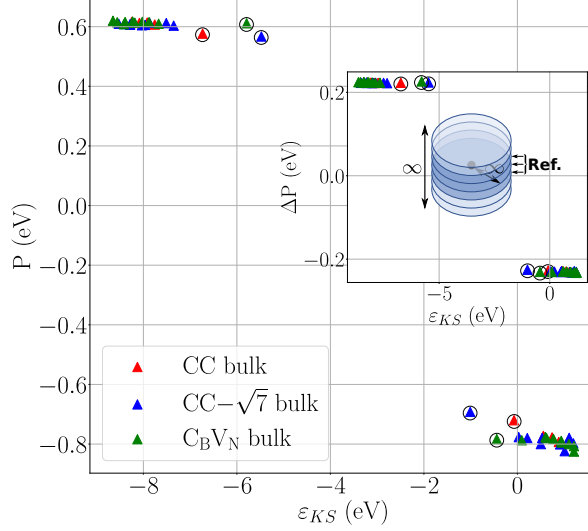


FIG. 9. Polarization energies from the monolayer to the bulk for a larger set of occupied and unoccupied states, including defect and h -BN delocalized states, as a function of Kohn-Sham energy with respect to the vacuum level. Defect states are circled. Most unoccupied states are unbound. (Inset) Evolution of the polarization from the 3-layer system (one undefected layer around the defected one) to the bulk.

the gap in the case of the CC, CC- $\sqrt{7}$ and $C_B V_N$ defects. The states are ordered according to their Kohn-Sham energy. The defect states are circled.

The salient result is that polarization energies for the occupied states at the top of the h -BN occupied states manifold are very stable around $P_e \sim 0.6$ eV, to be compared to the 0.57-0.61 eV shift obtained for the localized defect levels (see Fig. 8). As such, screening by additional layers hardly affects the difference of energy between localized defect levels and delocalized h -BN states at the top of the valence bands. Additional analysis in the SM [94], considering larger fragments, confirms that the polarization energy is hardly dependent on the in-plane localization of the considered states. This leaves hybridization and electrostatic effects in the ground-state as the only source able to modify significantly the position of the occupied defect levels with respect to the h -BN valence band maximum (VBM). Here again, polarization energies, difficult to obtain at the Kohn-Sham DFT level, are very much universal. Defect-dependent shifts with respect both to the vacuum level, but also the valence band maximum, can be obtained at the much cheaper (as compared to GW) Kohn-Sham DFT level.

As discussed above, the effect of stacking layers moves the defect occupied level towards the vacuum level (reduced ionization potential) by about 0.18 eV and 0.11 eV, respectively, at the

Kohn-Sham ground-state level for the CC and $C_B V_N$ defects. This correction is nearly entirely due to the interaction with nearest layers. Concerning h -BN, it has been shown and analyzed in several papers that the top of the valence band at K is very weakly dispersive in the AA' stacking configuration [104–106]. Namely, from the monolayer to the bulk, the top of the valence band remains degenerate, dispersion growing slowly away from the K -point. Taking the vacuum level as a reference, the top of the valence band at K was shown to go down in energy by about 0.1 eV [105] at the Kohn-Sham level with the HSE hybrid functional, demonstrating both weak electrostatic and hybridization effects. A similar value of 0.06 eV was found in Ref. 30 at the PBE level, confirming the stability of the valence band maximum at the Kohn-Sham ground-state level, namely in the absence of polarization effects between the monolayer and the bulk. Adding the -0.1 eV shift of the h -BN VBM and the +0.1 eV to +0.2 eV shift upward of the occupied defect levels in the CC and $C_B V_N$ cases, one finds that the energy spacing between the occupied defect levels and the VBM increases by a limited 0.2 eV to 0.3 eV from the monolayer to the bulk limit, an effect mostly related to electrostatics and hybridization effects accounted for at the Kohn-Sham level.

We finally address the challenging case of unoccupied states. Focusing first on the defect states, we observe in Fig. 9 that their polarization energy P_e is larger (in absolute value) as compared to that associated with occupied defect levels. Unoccupied defect states are approaching the vacuum level, being weakly bound to the atomic layer. As such, the associated wavefunctions starts delocalizing away from the atomic layer (see the analysis in the SM [94]), inducing an enhanced polarization response from neighboring layers. Considering the effect of adding screening layers beyond the nearest-neighbor layers (see Inset Fig. 9), namely calculating the polarization energy from the 3-layer system to the bulk, one observe that the effect of screening becomes much more state-independent and symmetric between holes and electrons. This is an indication that delocalization away from the defected layer remains small, at least for states close to the conduction edge, affecting mostly the response of the nearest layers but not beyond. This is similar to what was observed for the $C_B V_N$ defect with the out-of-plane C atom polarizing more strongly (as compared to the in-plane CC defect) the nearest layers. This overscreening effect due to loosely bound charges spilling out the BN layer vanishes quickly for the response of layers located farther away. As a result, polarization effects stabilize unoccupied defect levels by an energy $|P_e| \sim 0.7 - 0.8$ eV, or an energy $|P_e - P_h| \sim 1.3 - 1.4$ eV as compared to the h -BN valence band maximum.

We will not attempt here to discuss the position of the h -BN conduction band minimum. As shown in Fig. 9, states above the unoccupied defect levels lie above the vacuum with a positive

Kohn-Sham energy. As such, delocalized nearly-free-electron states are expected to be present at the conduction band minimum of *h*-BN as documented in early studies on *h*-BN [106, 107]. The difficulties associated with describing unbound states with localized basis sets, and the much larger dispersion of *h*-BN states upon stacking at the conduction band minimum [105, 106], are serious limitations for the present localized-basis fragments calculations. We report the reader to previous periodic-boundary *GW* and quantum Monte Carlo studies of the evolution of the electronic properties of pristine *h*-BN from the monolayer to the bulk [25, 31, 106, 108].

VII. CONCLUSION

We have introduced and validated a fragment *GW* approach for the study of defects in *h*-BN multilayer systems where individual layers are fragmented in domains with non-overlapping wave functions. The resulting interacting susceptibility and screened Coulomb potential are shown to accurately describe the screening properties of infinite monolayers in the vicinity of the dopant, reproducing at the few meV level the extrapolation of quasiparticle energies in the infinite layer size limit. Such a divide-and-conquer scheme allows to study at the many-body level systems containing thousands of atoms, dramatically facilitating the study of dilute defects in monolayer, few-layers, surface or bulk *h*-BN systems.

The success of the fragmentation scheme for the block-diagonalization of the independent-electron susceptibility is associated with the large ionic gap character of the *h*-BN substrate. For such systems, the response to a perturbation proceeds by the creation of very localized induced dipoles, rather than the displacement of electrons over large distances. This can be restated by saying that the susceptibility $\chi_0(\mathbf{r}, \mathbf{r}'; \omega)$ is very short-ranged, with an exponential decay in real-space in the case of insulators [109]. Along that line, exploring the robustness of this approach for other 2D systems with smaller gap (e.g. dichalcogenides) would be an interesting direction. In the present case, we find that our results are rather insensitive to fragment size and shape, provided that the fragments are large enough (around a hundred atoms in the present study). As an additional ingredient, passivation of edge atoms, by repelling edge states away from the host gap, reduces the spurious contribution of edge polarization as compared to the bulk one. We do not exclude more efficient passivation strategies.

As a first application, we have studied the evolution of the paradigmatic carbon-dimer and $C_B V_N$ defects energy levels from the monolayer to *n*-layer systems, including the surface and bulk

limits. The polarization energy, namely the evolution of the GW electronic energy levels as a function of increased screening upon adding additional layers, is shown to follow a nearly-universal $(\Delta P/n + P_\infty)$ law with the number $-n-$ of layers, where the rate ΔP and asymptotic value P_∞ depend on the defect location (bulk or surface) but hardly on the defect type. Such an approach rationalizes the evolution of defect energy levels as a function of the number of layers and allows to easily extrapolate data obtained for the monolayer or very-few layer systems to the bulk.

This universal behavior can be rationalized by emphasizing that the surrounding polarizable substrate reacts basically to an added charge associated with the photoemission process used to measure electron addition or removal energies. As such, the exact spatial distribution of this added charge, that depends on the defect type and chosen energy level, only contributes to higher order (dipolar, quadrupolar, etc.) terms to the perturbation felt by the polarizable substrate. While such arguments allow to rationalize asymptotic behaviors, it is remarkable that they start applying to the reaction of second, and even first, nearest-neighbor layers. While the present scheme ideally applies to localized defect states, our results suggest that similar polarization energies can be obtained for extended h -BN Bloch states, leaving aside conduction band edge states that start delocalizing away from the plane of atoms. Special care should probably be taken with defects inducing large elastic deformations, requiring potentially larger fragments.

Together with the fragmentation scheme, we have shown that the neglect of neighboring layer wave function overlap, a common approximation in the 2D-genomics approach, leads to underestimating screening effects by up to 10%. This error is however very largely canceled by neglecting the frequency dependence of the dielectric response in the calculation of the quasiparticle energy difference between the monolayer and n -layer systems. This approximation takes the form of the well-known static Coulomb-Hole plus screened exchange (COHSEX) approximation in the GW framework. This static Δ COHSEX schemes for calculating the increase in polarization energy upon adding layers, leads to overestimating polarization energies, significantly reducing the error introduced by decoupling wave function overlaps between layers.

We further explored a multipole-like expansion of the long-range susceptibility, with a dramatic reduction of the auxiliary basis size used to express density variations in the long-range. Together with fragmentation, this approach also contributed significantly to reducing the cost of performing many-body calculations. For sake of indication, COHSEX calculations on $\sim 10^5$ electrons, as encountered for 7-layer systems, were conducted with a typical cost of 1600 CPU hours in the present fragment approach. While done here in a somehow *ad hoc* fashion by removing high-angular

momentum channels in the auxiliary basis, such a scheme may certainly be improved.

Besides offering an alternative to periodic-boundary-condition calculations for study of the electronic properties of defect states in the dilute limit, the present scheme may offer a path to the study at the many-body level of disordered systems, including the stacking of layers of different chemical nature as in the field of 2D-genomics, but further the study of rotated layers with Moiré patterns [110], disordered monolayers such as *h*-BCN with the formation of segregated *h*-BN and graphene domains [111, 112], or disordered interfaces with organic systems or wet environments, with intriguing contribution of 2D substrate polarization modes to the interactions at the interface [113].

Finally, the present calculations of *GW* energy levels, accounting properly for long-range polarization effects, open the way to optical absorption calculations within the Bethe-Salpeter formalism, where excitonic electron-hole interactions are also expected to be screened by added layers.

ACKNOWLEDGMENTS

DA is indebted to ENS Paris-Saclay for his PhD fellowship. This work was performed using HPC resources from GENCI-IDRIS (Grant 2021-A0110910016). XB and ID acknowledge support from the French Agence Nationale de la Recherche (ANR) under contract ANR-20-CE29-0005.

-
- [1] A. Katzir, J. T. Suss, A. Zunger, and A. Halperin, *Phys. Rev. B* **11**, 2370 (1975).
 - [2] K. Era, F. Minami, and T. Kuzuba, *J. Lumin.* **24-25**, 71 (1981).
 - [3] M. G. Silly, P. Jaffrennou, J. Barjon, J.-S. Lauret, F. Ducastelle, A. Loiseau, E. Obraztsova, B. Attal-Tretout, and E. Rosencher, *Phys. Rev. B* **75**, 085205 (2007).
 - [4] L. Museur, E. Feldbach, and A. Kanaev, *Phys. Rev. B* **78**, 155204 (2008).
 - [5] S. Meuret, L. H. G. Tizei, T. Cazimajou, R. Bourrellier, H. C. Chang, F. Treussart, and M. Kociak, *Phys. Rev. Lett.* **114**, 197401 (2015).
 - [6] D. Wong, J. Velasco, L. Ju, J. Lee, S. Kahn, H.-Z. Tsai, C. Germany, T. Taniguchi, K. Watanabe, A. Zettl, F. Wang, and M. F. Crommie, *Nature Nanotech.* **10** (2015).

- [7] T. Tran, K. Bray, M. Ford, M. Toth, and I. Aharonovich, *Nature Nanotech* **11**, 37 (2016).
- [8] R. Bourrellier, S. Meuret, A. Tararan, O. Stéphan, M. Kociak, L. H. G. Tizei, and A. Zobelli, *Nano Lett.* **16**, 4317 (2016), pMID: 27299915, <https://doi.org/10.1021/acs.nanolett.6b01368>.
- [9] T. Q. P. Vuong, G. Cassabois, P. Valvin, A. Ouerghi, Y. Chassagneux, C. Voisin, and B. Gil, *Phys. Rev. Lett.* **117**, 097402 (2016).
- [10] N. R. Jungwirth, B. Calderon, Y. Ji, M. G. Spencer, M. E. Flatté, and G. D. Fuchs, *Nano Lett.* **16**, 6052 (2016), pMID: 27580074, <https://doi.org/10.1021/acs.nanolett.6b01987>.
- [11] A. Gottscholl, M. Kianinia, V. Soltamov, S. Orlinskii, G. Mamin, C. Bradac, C. Kasper, K. Krambrock, A. Sperlich, M. Toth, I. Aharonovich, and V. Dyakonov, *Nat. Mater.* **19**, 540 (2020).
- [12] F. Hayee, L. Yu, J. L. Zhang, C. J. Ciccarino, M. Nguyen, A. F. Marshall, I. Aharonovich, J. Vučkovič, P. Narang, T. F. Heinz, and J. A. Dionne, *Nat. Mater.* **19**, 534 (2020).
- [13] N. Mendelson, D. Chugh, J. R. Reimers, T. S. Cheng, A. Gottscholl, H. Long, C. J. Mellor, A. Zettl, V. Dyakonov, P. H. Beton, S. V. Novikov, C. Jagadish, H. H. Tan, M. J. Ford, M. Toth, C. Bradac, and I. Aharonovich, *Nat. Mater.* **20**, 321 (2021).
- [14] C. Attacalite, M. Bockstedte, A. Marini, A. Rubio, and L. Wirtz, *Phys. Rev. B* **83**, 144115 (2011).
- [15] C. Attacalite, L. Wirtz, A. Marini, and A. Rubio, *Sci. Rep.* **3** (2013).
- [16] N. Berseneva, A. Gulans, A. V. Krasheninnikov, and R. M. Nieminen, *Phys. Rev. B* **87**, 035404 (2013).
- [17] F. Wu, A. Galatas, R. Sundararaman, D. Rocca, and Y. Ping, *Phys. Rev. Mater.* **1**, 071001 (2017).
- [18] B. Huang and H. Lee, *Phys. Rev. B* **86**, 245406 (2012).
- [19] S. A. Tawfik, S. Ali, M. Fronzi, M. Kianinia, T. T. Tran, C. Stampfl, I. Aharonovich, M. Toth, and M. J. Ford, *Nanoscale* **9**, 13575 (2017).
- [20] G. Cheng, Y. Zhang, L. Yan, H. Huang, Q. Huang, Y. Song, Y. Chen, and Z. Tang, *Comput. Mater. Sci.* **129**, 247 (2017).
- [21] N. R. Jungwirth and G. D. Fuchs, *Phys. Rev. Lett.* **119**, 057401 (2017).
- [22] J. R. Reimers, A. Sajid, R. Kobayashi, and M. J. Ford, *J. Chem. Theory Comput.* **14**, 1602 (2018), pMID: 29412670, <https://doi.org/10.1021/acs.jctc.7b01072>.
- [23] M. Abdi, J.-P. Chou, A. Gali, and M. B. Plenio, *ACS Photonics* **5**, 1967 (2018), <https://doi.org/10.1021/acsphotonics.7b01442>.
- [24] L. Weston, D. Wickramaratne, M. Mackoït, A. Alkauskas, and C. G. Van de Walle, *Phys. Rev. B* **97**, 214104 (2018).

- [25] T. J. Smart, F. Wu, M. Govoni, and Y. Ping, *Phys. Rev. Mater.* **2**, 124002 (2018).
- [26] A. Sajid, J. R. Reimers, and M. J. Ford, *Phys. Rev. B* **97**, 064101 (2018).
- [27] M. E. Turiansky, A. Alkauskas, L. C. Bassett, and C. G. Van de Walle, *Phys. Rev. Lett.* **123**, 127401 (2019).
- [28] T. Korona and M. B. Chojecki, *Int. J. Quant. Chem.* **119**, e25925 (2019), <https://onlinelibrary.wiley.com/doi/pdf/10.1002/qua.25925>.
- [29] M. Mackoít-Sinkevičienė, M. Maciaszek, C. G. Van de Walle, and A. Alkauskas, *Appl. Phys. Lett.* **115**, 212101 (2019), <https://doi.org/10.1063/1.5124153>.
- [30] D. Wang and R. Sundararaman, *Phys. Rev. B* **101**, 054103 (2020).
- [31] Y. Chen and S. Y. Quek, *J. Phys. Chem. C* **125**, 21791 (2021), <https://doi.org/10.1021/acs.jpcc.1c07729>.
- [32] J. R. Reimers, J. Shen, M. Kianinia, C. Bradac, I. Aharonovich, M. J. Ford, and P. Piecuch, *Phys. Rev. B* **102**, 144105 (2020).
- [33] A. Sajid and K. S. Thygesen, *2D Mater.* **7**, 031007 (2020).
- [34] J. Bhang, H. Ma, D. Yim, G. Galli, and H. Seo, *ACS Appl. Mater. Interfaces* **13**, 45768 (2021), pMID: 34541839, <https://doi.org/10.1021/acsami.1c16988>.
- [35] C. Jara, T. Rauch, S. Botti, M. A. L. Marques, A. Norambuena, R. Coto, J. E. Castellanos-Águila, J. R. Maze, and F. Munoz, *J. Phys. Chem. A* **125**, 1325 (2021), pMID: 33554602, <https://doi.org/10.1021/acs.jpca.0c07339>.
- [36] M. Winter, M. H. E. Bousquet, D. Jacquemin, I. Duchemin, and X. Blase, *Phys. Rev. Mater.* **5**, 095201 (2021).
- [37] S. Gao, H.-Y. Chen, and M. Bernardi, *npj Comput. Mater.* **7**, 85 (2021).
- [38] F. Libbi, P. M. M. C. de Melo, Z. Zanolli, M. Verstraete, and N. Marzari, *arXiv*, 2111.03518.
- [39] C. Freysoldt, B. Grabowski, T. Hickel, J. Neugebauer, G. Kresse, A. Janotti, and C. G. Van de Walle, *Rev. Mod. Phys.* **86**, 253 (2014).
- [40] G. Miceli, W. Chen, I. Reshetnyak, and A. Pasquarello, *Phys. Rev. B* **97**, 121112 (2018).
- [41] L. Hedin, *Phys. Rev.* **139**, A796 (1965).
- [42] G. Strinati, H. J. Mattausch, and W. Hanke, *Phys. Rev. Lett.* **45**, 290 (1980).
- [43] M. S. Hybertsen and S. G. Louie, *Phys. Rev. B* **34**, 5390 (1986).
- [44] B. Farid, R. Daling, D. Lenstra, and W. van Haeringen, *Phys. Rev. B* **38**, 7530 (1988).
- [45] R. W. Godby, M. Schlüter, and L. J. Sham, *Phys. Rev. B* **37**, 10159 (1988).

- [46] M. P. Surh, H. Chacham, and S. G. Louie, *Phys. Rev. B* **51**, 7464 (1995).
- [47] M. Hedström, A. Schindlmayr, G. Schwarz, and M. Scheffler, *Phys. Rev. Lett.* **97**, 226401 (2006).
- [48] P. Rinke, A. Janotti, M. Scheffler, and C. G. Van de Walle, *Phys. Rev. Lett.* **102**, 026402 (2009).
- [49] L. Martin-Samos, G. Roma, P. Rinke, and Y. Limoge, *Phys. Rev. Lett.* **104**, 075502 (2010).
- [50] M. Jain, J. R. Chelikowsky, and S. G. Louie, *Phys. Rev. Lett.* **107**, 216803 (2011).
- [51] W. Chen and A. Pasquarello, *Phys. Rev. B* **88**, 115104 (2013).
- [52] A. Tararan, S. di Sabatino, M. Gatti, T. Taniguchi, K. Watanabe, L. Reining, L. H. G. Tizei, M. Kociak, and A. Zobelli, *Phys. Rev. B* **98**, 094106 (2018).
- [53] C. A. Rozzi, D. Varsano, A. Marini, E. K. U. Gross, and A. Rubio, *Phys. Rev. B* **73**, 205119 (2006).
- [54] F. Hüser, T. Olsen, and K. S. Thygesen, *Phys. Rev. B* **88**, 245309 (2013).
- [55] F. Aryasetiawan and O. Gunnarsson, *Rep. Prog. Phys.* **61**, 237 (1998).
- [56] B. Farid, *Electron Correlation in the Solid State - Chapter 3*, edited by N. March (Imperial College Press, London, 1999).
- [57] G. Onida, L. Reining, and A. Rubio, *Rev. Mod. Phys.* **74**, 601 (2002).
- [58] Y. Ping, D. Rocca, and G. Galli, *Chem. Soc. Rev.* **42**, 2437 (2013).
- [59] D. Golze, M. Dvorak, and P. Rinke, *Front. Chem.* **7**, 377 (2019).
- [60] R. Martin, L. Reining, and D. Ceperley, *Interacting Electrons: Theory and Computational Approaches* (Cambridge University Press, 2016).
- [61] T. Fujita and Y. Noguchi, *Phys. Rev. B* **98**, 205140 (2018).
- [62] J. Tölle, T. Deilmann, M. Rohlfing, and J. Neugebauer, *J. Chem. Theory Comput.* **17**, 2186 (2021), pMID: 33683119, <https://doi.org/10.1021/acs.jctc.0c01307>.
- [63] C. D. Spataru, *Phys. Rev. B* **88**, 125412 (2013).
- [64] K. Andersen, S. Latini, and K. S. Thygesen, *Nano Lett.* **15**, 4616 (2015), pMID: 26047386, <https://doi.org/10.1021/acs.nanolett.5b01251>.
- [65] K. T. Winther and K. S. Thygesen, *2D Mater.* **4**, 025059 (2017).
- [66] M. Drüppel, T. Deilmann, J. Noky, P. Marauhn, P. Krüger, and M. Rohlfing, *Phys. Rev. B* **98**, 155433 (2018).
- [67] F. Xuan, Y. Chen, and S. Y. Quek, *J. Chem. Theory Comput.* **15**, 3824 (2019), pMID: 31084031, <https://doi.org/10.1021/acs.jctc.9b00229>.
- [68] L. J. Sham and T. M. Rice, *Phys. Rev.* **144**, 708 (1966).
- [69] W. Hanke and L. J. Sham, *Phys. Rev. Lett.* **43**, 387 (1979).

- [70] G. Strinati, *Phys. Rev. Lett.* **49**, 1519 (1982).
- [71] B. Baumeier, M. Rohlfing, and D. Andrienko, *J. Chem. Theory Comput.* **10**, 3104 (2014), pMID: 26588281, <https://doi.org/10.1021/ct500479f>.
- [72] J. Li, G. D'Avino, I. Duchemin, D. Beljonne, and X. Blase, *J. Phys. Chem. Lett.* **7**, 2814 (2016), pMID: 27388926, <https://doi.org/10.1021/acs.jpcclett.6b01302>.
- [73] I. Duchemin, D. Jacquemin, and X. Blase, *J. Chem. Phys.* **144**, 164106 (2016), <https://doi.org/10.1063/1.4946778>.
- [74] I. Duchemin, C. A. Guido, D. Jacquemin, and X. Blase, *Chem. Sci.* **9**, 4430 (2018).
- [75] J. Wehner, L. Brombacher, J. Brown, C. Junghans, O. Çaylak, Y. Khalak, P. Madhikar, G. Tirimbò, and B. Baumeier, *J. Chem. Theory Comput.* **14**, 6253 (2018), pMID: 30404449, <https://doi.org/10.1021/acs.jctc.8b00617>.
- [76] L. Hedin, *Phys. Rev.* **139**, A796 (1965).
- [77] M. S. Hybertsen and S. G. Louie, *Phys. Rev. B* **34**, 5390 (1986).
- [78] B. Farid, R. Daling, D. Lenstra, and W. van Haeringen, *Phys. Rev. B* **38**, 7530 (1988).
- [79] I. Duchemin and X. Blase, *J. Chem. Theory Comput.* **16**, 1742 (2020), pMID: 32023052, <https://doi.org/10.1021/acs.jctc.9b01235>.
- [80] I. Duchemin and X. Blase, *J. Chem. Theory Comput.* **17**, 2383 (2021), pMID: 33797245, <https://doi.org/10.1021/acs.jctc.1c00101>.
- [81] J. B. Neaton, M. S. Hybertsen, and S. G. Louie, *Phys. Rev. Lett.* **97**, 216405 (2006).
- [82] F. Neese, *WIREs Comput. Mol. Sci.* **2**, 73 (2012).
- [83] D. Jacquemin, I. Duchemin, and X. Blase, *J. Chem. Theory Comput.* **11**, 3290 (2015), pMID: 26207104, <https://doi.org/10.1021/acs.jctc.5b00304>.
- [84] J. Li, G. D'Avino, I. Duchemin, D. Beljonne, and X. Blase, *J. Phys. Chem. Lett.* **7**, 2814 (2016), pMID: 27388926, <https://doi.org/10.1021/acs.jpcclett.6b01302>.
- [85] D. Jacquemin, I. Duchemin, and X. Blase, *J. Phys. Chem. Lett.* **8**, 1524 (2017), pMID: 28301726, <https://doi.org/10.1021/acs.jpcclett.7b00381>.
- [86] I. Duchemin, C. A. Guido, D. Jacquemin, and X. Blase, *Chem. Sci.* **9**, 4430 (2018).
- [87] J. L. Whitten, *J. Chem. Phys.* **58**, 4496 (1973), <https://doi.org/10.1063/1.1679012>.
- [88] X. Ren, P. Rinke, V. Blum, J. Wieferink, A. Tkatchenko, A. Sanfilippo, K. Reuter, and M. Scheffler, *New J. Phys.* **14**, 053020 (2012).
- [89] I. Duchemin, J. Li, and X. Blase, *J. Chem. Theory Comput.* **13**, 1199 (2017), pMID: 28094983,

- <https://doi.org/10.1021/acs.jctc.6b01215>.
- [90] R. Krishnan, J. S. Binkley, R. Seeger, and J. A. Pople, *J. Chem. Phys.* **72**, 650 (1980), <https://doi.org/10.1063/1.438955>.
- [91] J. P. Perdew, M. Ernzerhof, and K. Burke, *J. Chem. Phys.* **105**, 9982 (1996), <https://doi.org/10.1063/1.472933>.
- [92] F. Weigend, *Phys. Chem. Chem. Phys.* **8**, 1057 (2006).
- [93] P. Auburger and A. Gali, *Phys. Rev. B* **104**, 075410 (2021).
- [94] See Supplemental Material at [Link to be added upon publication] for (I) the relaxed structures studied in the main manuscript, (II) the evolution with distance and for several directions of the ratio of the statically screened Coulomb potential over the bare Coulomb potential, (III) microelectrostatic studies of polarization energies on the basis of system size varying over several order of magnitude, (IV) the evolution of the $C_B V_N$ quasiparticle gap as a function of the number of layers in the bulk geometry, (V) the evolution of the CC occupied level polarization energy as a function of the number of layers with the defect located in the subsurface and subsurface, respectively, (VI) the evolution of the *h*-BN states polarization energy as a function of the fragment size over which they are confined, and in (VII) a study of the delocalization away from the atomic plane of unoccupied states.
- [95] A. Sajid, M. J. Ford, and J. R. Reimers, *Rep. Prog. Phys.* **83**, 044501 (2020).
- [96] V. Solozhenko, G. Will, and F. Elf, *Solid State Commun.* **96**, 1 (1995).
- [97] W. Paszkowicz, J. Pelka, M. Knapp, T. Szyszko, and S. Podsiadlo, *Appl. Phys. A* **75**, 431 (2002).
- [98] S. Grimme, J. Antony, S. Ehrlich, and H. Krieg, *J. Chem. Phys.* **132**, 154104 (2010), <https://doi.org/10.1063/1.3382344>.
- [99] G. D'Avino, L. Muccioli, F. Castet, C. Poelking, D. Andrienko, Z. G. Soos, J. Cornil, and D. Beljonne, *J. Phys. : Cond. Matt.* **28**, 433002 (2016).
- [100] P. Cudazzo, C. Attaccalite, I. V. Tokatly, and A. Rubio, *Phys. Rev. Lett.* **104**, 226804 (2010).
- [101] P. Cudazzo, I. V. Tokatly, and A. Rubio, *Phys. Rev. B* **84**, 085406 (2011).
- [102] S. Latini, T. Olsen, and K. S. Thygesen, *Phys. Rev. B* **92**, 245123 (2015).
- [103] G. D'Avino, L. Muccioli, C. Zannoni, D. Beljonne, and Z. G. Soos, *J. Chem. Theory Comput.* **10**, 4959 (2014), pMID: 26584380, <https://doi.org/10.1021/ct500618w>.
- [104] R. M. Ribeiro and N. M. R. Peres, *Phys. Rev. B* **83**, 235312 (2011).
- [105] D. Wickramaratne, L. Weston, and C. G. Van de Walle, *J. Phys. Chem. C* **122**, 25524 (2018), <https://doi.org/10.1021/acs.jpcc.8b09087>.

- [106] F. Paleari, T. Galvani, H. Amara, F. Ducastelle, A. Molina-Sánchez, and L. Wirtz, *2D Mater.* **5**, 045017 (2018).
- [107] X. Blase, A. Rubio, S. G. Louie, and M. L. Cohen, *Europhys. Lett.* **28**, 335 (1994).
- [108] R. J. Hunt, B. Monserrat, V. Zólyomi, and N. D. Drummond, *Phys. Rev. B* **101**, 205115 (2020).
- [109] This property stems from the real-space behaviour of the constituting hole and electron one-body Green's functions (see Ref. 114).
- [110] E. M. Alexeev, D. A. Ruiz-Tijerina, M. Danovich, M. J. Hamer, D. J. Terry, P. K. Nayak, S. Ahn, S. Pak, J. Lee, J. I. Sohn, M. R. Molas, M. Koperski, K. Watanabe, T. Taniguchi, K. S. Novoselov, R. V. Gorbachev, H. S. Shin, V. I. Fal'ko, and A. I. Tartakovskii, *Nature* **567**, 81 (2019).
- [111] M. Bernardi, M. Palummo, and J. C. Grossman, *Phys. Rev. Lett.* **108**, 226805 (2012).
- [112] M. Bernardi, M. Palummo, and J. C. Grossman, *ACS Nano* **6**, 10082 (2012), pMID: 23062107, <https://doi.org/10.1021/nn303815z>.
- [113] N. Kavokine, M. Bocquet, and L. Bocquet, *Nature* **602**, 84 (2022).
- [114] A. Schindlmayr, *Phys. Rev. B* **62**, 12573 (2000).

Supplemental Material for :

Universal polarisation energies for defects in monolayer, surface and bulk hexagonal boron nitride : A finite-size fragments *GW* approach

We provide here below supplemental informations concerning (I) the relaxed structures studied in the main manuscript, (II) the evolution with distance and for several directions of the ratio of the statically screened Coulomb potential over the bare Coulomb potential, (III) microelectrostatic studies of polarization energies on the basis of system sizes varying over several orders of magnitude, (IV) the evolution of the $C_B V_N$ quasiparticle gap as a function of the number of layers in the bulk geometry, (V) the evolution of the CC occupied level polarization energy as a function of the number of layers with the defect located in the subsurface and subsurface, respectively, (VI) the evolution of the h -BN states polarization energy as a function of the fragment size over which they are confined, and in (VII) a study of the delocalization away from the atomic plane of unoccupied states.

I. RELAXED STRUCTURES

We provide in Fig. [S1](#) a ball-and-stick representation of the carbon-dimer (CC) defect at the center of BN flakes containing 138, 202 and 278 atoms. Edge atoms are passivated by hydrogens (in white). Structures have been relaxed at the 6-311G(d) PBE0-D3 level. Such systems are used to extrapolate to infinity the quasiparticle band gap of the CC dimer defect in the infinite size monolayer limit that is used as reference for the fragment approach (see Fig. 3 main manuscript).

We further represent in Fig. [S2](#) the $C_B V_N$ defect at the center of a BN86 flake in a monolayer, bilayer and trilayer geometry (AA' stacking). The relaxed monolayer displays a dramatically distorted non-planar structure, as a result presumably of the strain generated by the B-B bond across the nitrogen vacancy. However, the interaction with a second layer [Fig. [S2\(b\)](#)] restores planarity but with a C atom that goes off-plane by about 0.55 Å. The corrugation of the defected layer, that is the maximum out-of-plane displacement of B/N atoms, is of the order of 0.25 Å. The addition of a 3rd layer [Fig. [S2\(c\)](#)] leads to the same geometry, with the C atom that goes off-plane by about 0.52 Å and a reduced corrugation of 0.22 Å. In the main manuscript, when studying the evolution of the electronic energy levels from the monolayer to a n -layer system in the surface configuration

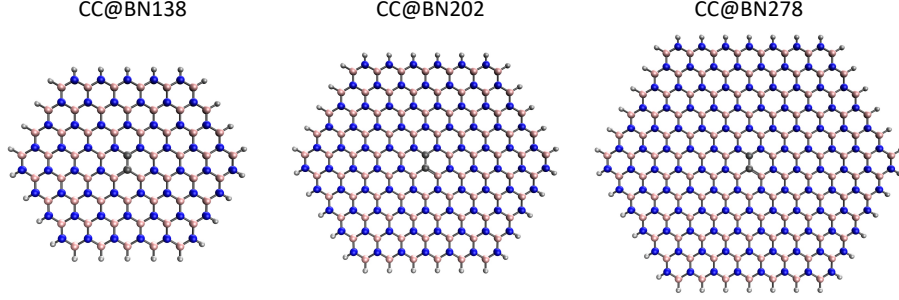


FIG. S1. Representation of the C2@BN138, C2@BN202 and C2@BN278 structures. Hydrogen, boron, carbon and nitrogen atoms are in white, pink, black, and blue, respectively. Structures are not on scale.

(defect at the surface), the monolayer geometry is extracted from the bilayer one. Similarly, when studying the evolution of the electronic energy levels from the monolayer to a n -layer system in the bulk configuration, the monolayer geometry is extracted from the trilayer geometry.

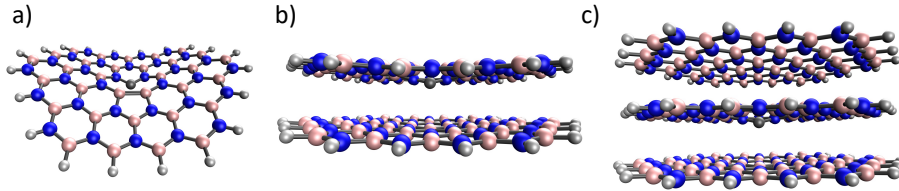


FIG. S2. Representation of the $C_B V_N$ defect in (a) a BN86 monolayer, (b) a BN86 bilayer, and (c) a BN86 trilayer. Structures are not on scale.

II. SCREENED COULOMB POTENTIAL $W(\mathbf{r}, \mathbf{r}'; \omega = 0)$ ALONG SPECIFIC DIRECTIONS

We plot in Fig. S3 the ratio of the statically screened Coulomb potential $W(\mathbf{r}, \mathbf{r}'; \omega = 0)$ divided by the bare Coulomb potential V in the case of the carbon-dimer defect with \mathbf{r} located at the center of the CC bond and \mathbf{r}' displaced along specific directions. In the main text, the plot was provided along the \vec{u}_y direction. The small variations for a given $|\mathbf{r} - \mathbf{r}'|$ distance indicate the magnitude of local field effects that fade away at large distance. We observe that there is no screening at short range [W/V goes to unity for $|\mathbf{r} - \mathbf{r}'| \rightarrow 0$] and that further in the h -BN monolayer there is no screening in the long-range [W/V goes to unity for $|\mathbf{r} - \mathbf{r}'| \rightarrow +\infty$] as documented in several analytic studies [54, 100–102].

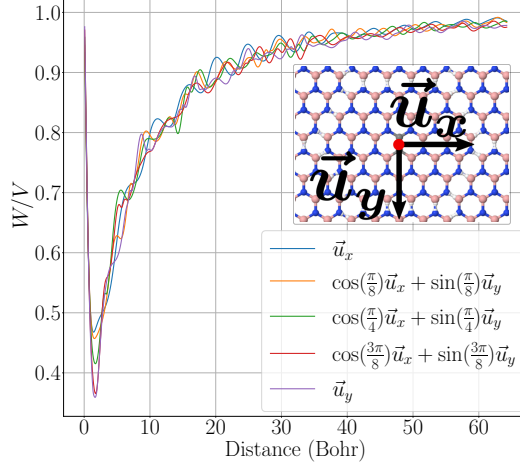


FIG. S3. Representation of the ratio of the static screened Coulomb potential $W(\mathbf{r}, \mathbf{r}'; \omega = 0)$ divided by the bare Coulomb potential V along several directions for \mathbf{r}' with \mathbf{r} fixed to the center of the defect CC bond.

III. MICROELECTROSTATIC STUDY OF SCALING LAWS IN THE VERY LARGE SYSTEM SIZE LIMIT

To validate the infinite size extrapolations performed on the basis of *ab initio* calculations, we adopt a microelectrostatic semi-empirical approach allowing to study systems comprizing up to ~ 78000 atoms/layer. Such studies confirm the accuracy of extrapolations based on data acquired at the *ab initio* level on systems comprizing a few thousand atoms. In brief, B/N atoms are replaced by polarizable centers equipped with an atomic polarizability fitted to reproduce the RPA polarizability of the BNX (X=86, 138, 202, etc.) clusters (see Fig. 4 of the main manuscript). In the presence of the field generated by a charge associated with the CC@BN86 defect levels, as given by *ab initio* calculations, induced dipoles are generated on these polarizable centres. The energy of these dipoles, interacting with the source charge and with each other, is minimized. The reaction field of these equilibrated dipoles on the source charges gives the polarization energy. In such calculations, only the polarization energy, not the ground-state electrostatic and hybridization effects, are accounted for. Such a scheme is implemented in the MESCAL code [99, 103].

We plot in Fig. S4 the semi-empirical polarization energy contributing to the closing of the CC@BN86 defect-associated gap (namely $\Delta_{\text{gap}} = P_e - P_h$) as a function of system size (number of polarizable centers N_{at} per layer). Taking the case of the monolayer, the semi-empirical polarization energy leads to a difference in gap from the CC@BN86 fragment to the infinite monolayer of 0.41 eV, in close agreement with the *ab initio* data that predict a 0.46 eV gap evolution (see Fig. 3

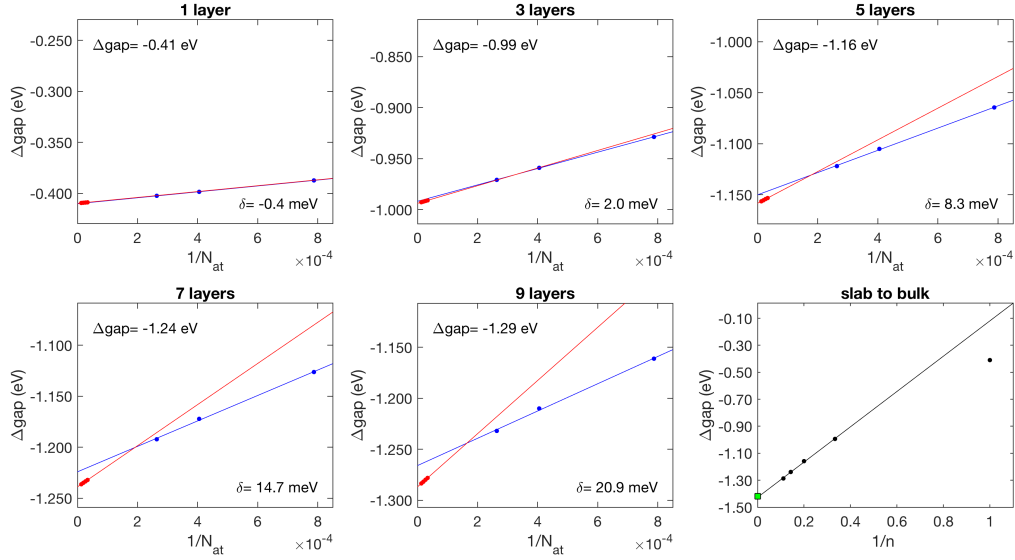


FIG. S4. Evolution of the gap between the occupied and unoccupied CC defect energy levels with the system size, computed with a classical induced-dipole model of atomistic resolution for 2D slabs of a given thickness (up to $n = 9$ layers, the defect is placed in the middle layer), and as a function of the number of layers (last panel). Slab calculations: blue points are results obtained on systems of roughly the same size (up to $N_{at} = 3768$ atoms/layer) as those employed in the fragment COHSEX calculations in the manuscript (Figure 7); red points refer to results obtained on much larger systems (up to $N_{at} = 78166$ atoms/layer); lines are linear regressions performed on the two data sets. The difference between the two intercepts δ (noted in the bottom-right corner of each plot) quantifies the error associated with the extrapolation on relatively-small systems. This error is negligible for the monolayer and grows with the slab thickness reaching 20.9 meV for the 9-layer system. The gap variation extrapolated in the infinite slab limit is noted in the top-left corner of each panel. The last panel shows the evolution of the gap variation as a function of the film thickness (black dot), converging linearly in $1/n$ to the bulk value (green square), the latter obtained upon extrapolating results for spheres of increasing radius.

main manuscript) with a 0.05 eV contribution from the evolution of Kohn-Sham eigenvalues not accounted for in the semi-empirical approach. We compare the $(1/N_{at})$ extrapolation obtained on the basis of data points acquired for system sizes equivalent to that used in the *ab initio* calculations (blue dots and fits), namely a central CC@BN86 cluster surrounded by up to 4th nearest-neighbour pristine BN86 fragments, to calculations and fits (in red) obtained with systems more than an order of magnitude larger. In the monolayer and trilayer cases, the difference is within the meV,

confirming that systems used at the *ab initio* level are large enough to obtain a reliable extrapolation. This difference becomes larger when the number of layer increases but remains within 15 meV up to the 7-layer systems studied in the main manuscript. It is a general result that convergence criteria rely on the aspect ratio (radius versus height) in the case of cylinders. Finally (lowest right "slab to bulk" plot), the $(1/n)$ behavior with layer number n of the polarization energy is confirmed using the microelectrostatic model. We observe that the ($n = 3$) case is already on the $(1/n)$ fit.

IV. MONOLAYER TO BULK QUASIPARTICLE GAP EVOLUTION FOR THE $C_B V_N$ DEFECT

We present in Fig. S5 the evolution of the $C_B V_N$ quasiparticle gap, taking as a reference the monolayer, as a function of the number of layers for the $C_B V_N$ defect in the bulk limit. Layers are added on each side alternatively of the central defected layer, respecting AA' stacking. The defected layer geometry, with the C atom located $\sim 0.52 \text{ \AA}$ off-plane, has been relaxed using a 3-layer geometry within the DFT 6-311G(d) PBE0+D3 approach. In the fragment approach, the evolution of the gap properly contains the -40 meV and -57 meV evolution (closing) at the Kohn-Sham level from the monolayer to the bi- and trilayers, respectively, additional layers hardly changing the Kohn-Sham gap value. As such, both ground-state electrostatic and hybridization effects, together with polarization (screening) effects at the many-body level, are accounted for.

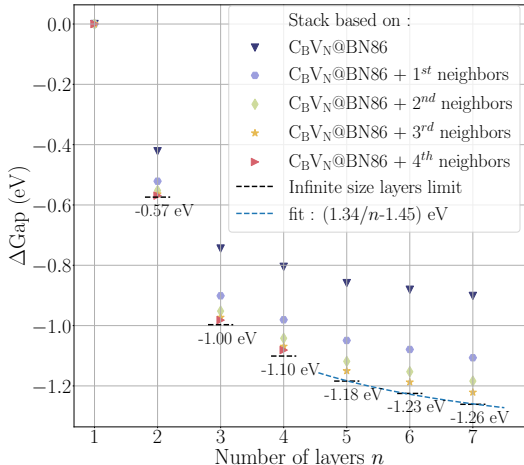


FIG. S5. Evolution of the quasiparticle gap as a function of the number of layers and as compared to the monolayer for the $C_B V_N$ defect in the bulk geometry (layers successively added on both side of the defect).

V. POLARIZATION ENERGY FOR DEFECTS IN SUB(SUB)SURFACE POSITION

We complete our study by considering in Fig. S6 the evolution of the occupied defect level polarization energy for the CC dimer defect from the monolayer to a n -layer system with the defect in subsurface and subsurface positions. In the subsurface case, the ($n=2$) layer is added on one side of the defected layer, all layers for ($n > 2$) being added on the other side. In the subsurface case, the layers are added alternatively on each side of the defected layer up to $n=5$ (2 layers on each side) and then added subsequently only on one side. The $P_\infty=0.54$ eV polarization energy for the subsurface position can be compared to $P_\infty=0.58$ eV for the bulk position (see Fig. 8a main manuscript). The surface case is reproduced from Fig. 8a main manuscript for sake of comparison.

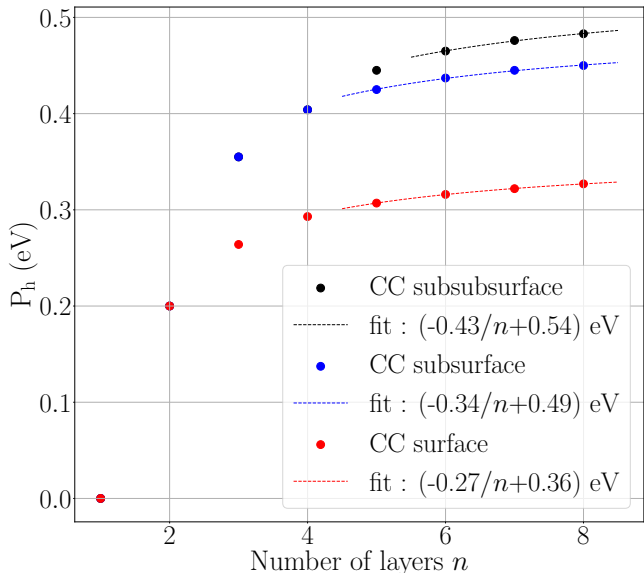


FIG. S6. Polarization energy as compared to the monolayer for the CC dimer defect occupied level. Both the subsurface and subsurface positions are explored.

VI. POLARIZATION ENERGY OF h -BN STATES AS A FUNCTION OF FRAGMENT SIZE

We test in the present Section the evolution of the polarization energy associated with the highest occupied h -BN delocalized states as a function of the fragment size. Since in our approach the h -BN states are confined to the central fragment, varying the size of such a fragment, from BN86 to BN138, allows to assess the influence of the in-plane spatial extension. In Fig. S7, we compare the polarization energies obtained for the highest occupied (HOMO) orbital of pure (undefected)

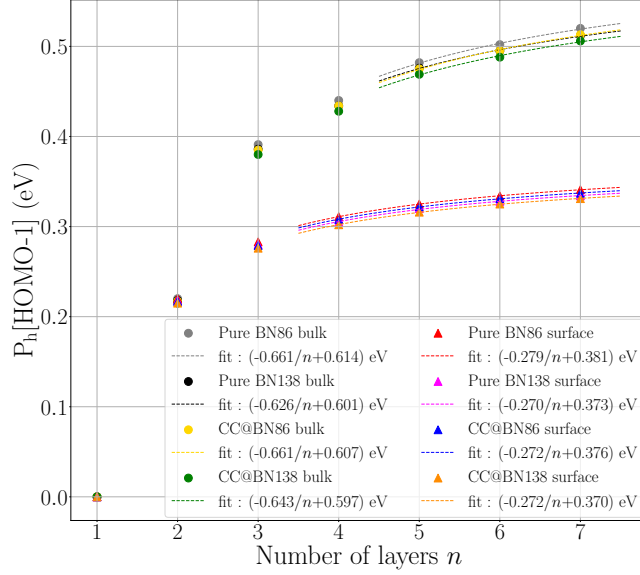


FIG. S7. Polarization energies for the monolayer to a n -layer system for the highest occupied h -BN state delocalized over a central fragment with size BN86 or BN138. Both the highest occupied (HOMO) orbital of a pristine (pure) central BN86 or BN138 fragments, and the highest-but-one (HOMO-1) orbital of defected CC@BN86 or CC@BN138 fragments, are studied in the bulk and surface limits.

central BN86 and BN138 clusters, surrounded by fragments of the same size in the same layer or in surrounding layers. As in the main text, we also look at the evolution of the highest-but-one (HOMO-1) occupied orbital of defected central CC@BN86 and CC@BN138 clusters. Both the surface and bulk limits are considered. Variations of the order of 10 meV are observed, from $P_h \simeq 0.61 \text{ eV}$ to $P_h \simeq 0.60 \text{ eV}$ in the bulk limit, confirming the stability of the obtained polarization energies for extended h -BN Bloch states as a function of fragment size.

VII. LOCALIZATION OF UNOCCUPIED VERSUS OCCUPIED STATES

We plot in Fig. S8 the charge density accumulated within a distance $-z$ - of a CC@BN86 defected system for selected states. Only the charge on one side of the atomic layer is accounted for. The graph evidences the delocalization away from the atomic plane with increasing Kohn-Sham energy. This can be used as a mean to better understand the increase of polarization energies (in absolute value) for unoccupied states with increasing energies. As discussed in the main text, this delocalization affects mainly the polarization response from the nearest-neighbor layers, additional screening originating from layers added beyond being nearly independent of the chosen state,

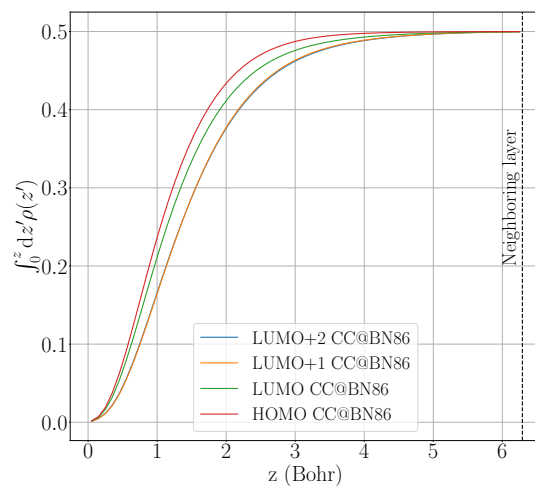


FIG. S8. Integrated charge accumulated within a distance $-z-$ of a CC@BN86 defected fragment for various states. HOMO indicates the highest occupied orbital, while LUMO, (LUMO+1) and (LUMO+2) indicate the lowest, lowest-plus-one and lowest-plus-two unoccupied ones. The vertical dashed line indicates the position of the neighboring layer.

restoring the electron-hole polarization energy symmetry.